Supplementary Information

Engineering grain boundaries in monolayer molybdenum disulfide for an efficient water/ion separation

Jie Shen[1†], Areej Aljarb[2†], Yichen Cai[3†], Xing Liu[4†], Jiacheng Min[5†], Yingge Wang[1], Chenhui Zhang[3], Cailing Chen[1], Mariam Hakami[3], Jui-Han Fu[6], Hui Zhang[7,8], Guanxing Li[1], Xiaoqian Wang[1], Zhuo Chen[1], Jiaqiang Li[1], Xinglong Dong[1], Vincent Tung[3,6*], Guosheng Shi[4,9*], Ingo Pinnau[1*], Lain-Jong Li[5*], and Yu Han[1*]

[1]King Abdullah University of Science and Technology (KAUST), Physical Sciences and Engineering Division (PSE), Advanced Membranes and Porous Materials (AMPM) Center, Thuwal 23955-6900, Saudi Arabia

[2]Department of Physics, King Abdulaziz University, Jeddah 21589, Saudi Arabia

[3]King Abdullah University of Science and Technology (KAUST), Physical Sciences and Engineering Division (PSE), Thuwal 23955-6900, Saudi Arabia

[4]Shanghai Applied Radiation Institute, State Key Lab. Advanced Special Steel, Shanghai University, Shanghai 200444, P. R. China

[5]Department of Mechanical Engineering, and Department of Physics, University of Hong Kong, Pok Fu Lam Road, Hong Kong 518057, P. R. China

[6]Department of Chemical System Engineering, School of Engineering, The University of Tokyo, Tokyo 113-8656, Japan

[7]Electron Microscopy Center, South China University of Technology, Guangzhou 510640, China

[8]School of Emergent Soft Matter, South China University of Technology, Guangzhou 510640, China

[9]Key Laboratory of Comprehensive and Highly Efficient Utilization of Salt Lake Resources, Qinghai Institute of Salt Lakes, Chinese Academy of Sciences, Xining, Qinghai 810008, PR China

[†]These authors contributed equally

*E-mail: vincent.tung@kaust.edu.sa; gsshi@shu.edu.cn; ingo.pinnau@kaust.edu.sa; lanceli1@hku.hk; yu.han@kaust.edu.sa

Experimental Section

Growth of monolayer MoS_2 films. Monolayer C-MoS_2 films were grown on sapphire wafers using the CVD method in a two-zone furnace using MoO_3 (≥99.5% purity from Sigma-Aldrich) and sulfur powder (≥99.5 % purity from Sigma-Aldrich) as the precursors. The standard CVD growth conditions for C-MoS_2-6.8 were: 4 g of sulfur powder upstream at 160 °C (the first zone), 0.8 g of MoO_3 in a ceramic boat at the center of the furnace (the second zone), a 2-inch (0001) sapphire wafer downstream, 30 Torr chamber pressure, 70 standard cubic centimeters per minute of Ar flow, and heating of the second zone from room temperature to 750 °C at 43 °C/min, held for 5 min (seed alignment), then to 800 °C at 17 °C/min, and held for 8 min.

The average grain size of C-MoS_2 was tuned by varying the heating temperature of sulfur (i.e., the first zone). Specifically, C-MoS_2-443, C-MoS_2-87.3, and C-MoS_2-0.26 were prepared by setting the temperature of the first zone to 145, 150, and 175 °C, respectively, while keeping the other standard conditions unchanged. Monolayer R-MoS_2 films (i.e., R-MoS_2-7.4) were prepared using the standard conditions described above for C-MoS_2-6.8, except that the seed alignment step was omitted.

MoS_2 membrane fabrication. PDMS, used for the MoS_2 transfer process, was prepared by thoroughly mixing a silicone base (Sylgard 184) and curing agent (Sylgard) in a ratio of 10:1 (wt:wt) (Dow Corning Corporation, USA). After degassing for 30 min, we slowly poured the PDMS solution (~33 g) over a clean silicon wafer in a Petri dish, followed by degassing for ~10 min to remove trapped air bubbles and baking at 80 °C for 4 h. Then, the PDMS film (~1.5 mm thickness) was carefully detached from the silicon wafer and placed on the top of MoS_2/sapphire. Conformal contact between PDMS and MoS_2/sapphire without compression was ensured to avoid cracks and large amounts of PDMS residues on the MoS_2 surface. Next, we dropped deionized (DI) water around the edge of MoS_2/sapphire to enable capillary force-driven water penetration into the interface between hydrophobic MoS_2 and hydrophilic sapphire. The stacked PDMS/MoS_2/sapphire sample was then immersed in a 1 M KOH aqueous solution at 40 °C for an hour. PDMS/MoS_2 was detached from the sapphire substrate and carefully washed by DI water. After maintaining the detached PDMS/MoS_2 sample at room temperature for ~30 min to remove the extra water, it was carefully placed on top of a porous PC substrate (50 nm pore size, ~1.2 % porosity, Dubach International B.V., Netherland). PDMS was attached to a stiff backing [thermal release tape (TRT), 0.5 mm thick, Nitto Denko Corporation, Japan] to prevent elongation during the peeling process. The PC substrate was attached to a silicon wafer by another TRT (Supplementary Fig. 9). During the transfer process, PDMS was peeled off by a motorized machine (Model F755, Mark-10 Corporation, USA) at a constant speed of 0.5 μm s^{-1}, leaving the MoS_2 layer on the PC substrate. The MoS_2/PC membrane was finally released by heating at 80 °C for 20 s to remove the TRT.

The MoS_2 monolayers were also transferred onto porous AAO (20 nm pore size, ~50 % porosity, Sterlitech, USA). Before use, the AAO substrate was polished with a diamond lapping film (Ted Pella, USA, grade: 100 nm) for 90 s, followed by soaking in a 10 wt% sulfuric acid solution for 30 s to dissolve the alumina dust, and then rinsed with DI water. The polishing pressure and acid exposure time were carefully controlled to avoid damaging the AAO substrates. Next, polymethyl methacrylate (950 PMMA A4, MICROCHEM, USA) was spin-coated on MoS_2/sapphire at a speed of 2,000 rpm, and the resulting PMMA-coated MoS_2/sapphire sample was then baked at 70 °C for 10 min. The same procedure was repeated three times. The PMMA/MoS_2/sapphire sample was soaked in a 1 M KOH aqueous solution at 40 °C for an hour to detach the PMMA/MoS_2 layer from the sapphire substrate. After washing by DI water, the PMMA/MoS_2 layer was transferred onto an AAO substrate, followed by drying at room temperature for ~12 h and washing off the PMMA coating by acetone. Notably, the temperature involved in the above processes should not be higher than the glass transition temperature of PMMA, i.e., ~100 °C, to maintain the high quality of the transferred MoS_2 films. The occasional pinholes were sealed by an established interfacial polymerization (IP) method[1,2] using an unstirred 5 mL Franz cell (Permegear Inc.) with a 9 mm orifice. The membrane was placed between the upper and lower compartments, which were filled with a 0.001 wt% hexamethylenediamine (Sigma Aldrich) aqueous solution and a 0.002 wt% trimesoyl chloride (Sigma Aldrich) *n*-hexane solution, respectively. The reaction was allowed to continue for 5 h and then stopped by pipetting out all the solution from the cell. The membrane surface was then thoroughly washed with *n*-hexane and ethanol, followed by overnight air-drying.

Monolayer MoS_2 membranes supported by silicon nitride (SiN_x) substrates with a single hole were fabricated for the nanofluidic experiments and AFM-nanoindentation tests. First, we fabricated a 100-nm-thick low-stress SiN_x membrane on both sides of a silicon wafer (~300 μm thick) using the low-pressure chemical vapor deposition (LPCVD) method. Reactive ion etching (RIE) was employed to remove a 1 × 1 mm^2 section from one of the SiN_x layers. After exposure to KOH (25 wt%), the silicon layer was removed, leaving a free-standing SiNx membrane on the other side (approximately 100 × 100 μm^2). A circular hole with an aperture diameter of 5 μm was then etched in the free-standing SiN_x membrane by RIE. Next, the MoS_2 film was transferred by the PDMS-assisted method using a micromanipulator to cover the hole in the SiN_x membrane. Next, epoxy coating (Devcon®) was carefully performed around the MoS_2 membrane under an optical microscope to seal any hole and improve the dielectric properties of the substrate[3].

Water and ion transport measurements. Water and ion transport driven by osmotic pressure were evaluated using a forward osmosis (FO) system, described in our previous work[4], and the MoS_2 membranes fabricated on porous PC substrates. The membrane was placed in between the feed side and draw side compartments of a customized 10 mL side-by-side glass

diffusion cell (Permegear, Inc., USA). During each measurement, both the feed and draw sides were magnetically stirred to minimize concentration polarization.

For the water transport experiments, we used a 0.1–2 M NaCl aqueous solution in the draw side and DI water of the same volume in the feed side, and subsequently sealed the glass cell with a Teflon® stopper on each side. The selective layer of the membrane was placed facing the draw-side solution. The water flux (J_w, mol m^{-2} h^{-1}) was derived from the changes in the liquid volume of the draw side (ΔV, ml) with time (Δt, h) and membrane area (A_m, m^2) according to equation (S1):

$$J_w = \frac{\Delta V \rho_w}{M_{mol} A_m \Delta t} \quad \text{(S1)}$$

where ρ_w (g mL^{-1}) is the density of water at 25 °C, M_{mol} is the molar mass of water.

The ion transport measurements were performed by filling the two compartments of the cell with equivalent volumes of 2 M sucrose (draw side) and 0.1–0.6 M aqueous salt solutions (feed side, KCl, NaCl, $CaCl_2$, $MgCl_2$ or $AlCl_3$). The selective layer of the membrane was placed facing the feed-side salt solution. The ion permeation in the synthetic seawater through the membrane was measured by using a mixture of aqueous solutions of KCl (0.0093 M), NaCl (0.42 M), Na_2SO_4 (0.029 M), $CaCl_2$ (0.011 M) and $MgCl_2$ (0.056 M) on the feed side, and a 2 M sucrose solution on the draw side. The change in the ionic conductivity change was continuously recorded using an ionic conductivity meter (Thermo Scientific Orion Star A210). The salt concentration (C, mol L^{-1}) was determined from the measured ionic conductivity (k, S m^{-1}) using equation (S2):

$$C = \frac{1}{1000} \cdot \frac{k}{\Lambda_m} \quad \text{(S2)}$$

where Λ_m (S m^2 mol^{-1}) is the molar conductivity. In addition, the concentrations of the cations were measured by inductively coupled plasma–optical emission spectrometry (ICP-OES, 7200-ES, Varian, Inc./Agilent). The ion flux (J_s, mol m^{-2} h^{-1}) was calculated using equation (S3):

$$J_s = \frac{C V}{A_m \Delta t} \quad \text{(S3)}$$

where V is the effective volume of the solution on the draw side. The water/ion selectivity α_w was obtained as follows:

$$\alpha_w = \frac{J_w}{J_s} \quad \text{(S4)}$$

To ensure a long-term continuous operation in the FO system, the salt solution in the feed compartment was replenished to compensate for the loss due to sample extraction from the permeate compartment. The salt rejection was calculated using the following relation:

$$R = 1 - \frac{(C_{d,i} + \Delta C_d) \times (V_{d,i} + \Delta V) - C_{d,i} V_{d,i}}{C_{f,i} \Delta V} \quad \text{(S5)}$$

where $V_{d,i}$ is the initial volume of the draw side, ΔV is the increased volume of the draw side, $C_{d,i}$ is the initial salt concentration on the draw side, ΔC_d is the increase in the salt concentration on the draw side, $C_{f,i}$ is the initial salt concentration on the feed side, and $C_{f,i}\Delta V$ indicates the amount of salt that would have permeated in the case of zero rejection.

Hydrostatic-pressure-driven transport measurements were performed on the AAO-supported MoS_2 membranes using a home-made reverse osmosis (RO) apparatus with a dead-end configuration under pressures up to 13 bar. Before the measurements, the flow of water through the membranes was stabilized for approximately 1 h to ensure a steady state. The permeated water was collected and weighed at specific time intervals to calculate the hydraulic permeance. The driving force was calculated by excluding the osmotic pressure difference ($\Delta\pi$) across the membrane, with respect to the applied hydraulic pressure. The conductivity of the permeate solution was measured to calculate the salt rejection of the membrane.

Proton and ion transport were studied by measuring the *I*-*V* curves using an electrochemical workstation (Autolab PGSTAT 302N, Switzerland), and the SiN_x-supported MoS_2 membranes. Two Ag/AgCl electrodes with a salt bridge (3 M KCl) were used to eliminate the redox potential difference[4]. The voltage was swept from -200 mV to 200 mV with a voltage step of 20 mV to reduce the risk of damage, and the acquisition time for each preset voltage was set as 5 s to avoid transient hysteresis after changing the voltage. All the measurements were conducted at room temperature. The areal conductance (G) was calculated using the equation: $G = I / (V \times A)$, where I is the current, V is the voltage, and A is the area of the single aperture on the SiN_x membrane that was covered by the MoS_2 membrane.

DFT calculations. The DFT calculations were performed using the Vienna ab initio simulation package. The projector augmented wave method was used to describe the electron–ion interactions[5,6], and the gradient-corrected Perdew–Burke–Ernzerh functional was adopted to describe the electron exchange and correlation energy. The cutoff energy for the plane-wave basis set was set as 520 eV, and the total energy convergence was set to be lower than 1×10^{-6} eV, with a force convergence of 0.02 eV/Å for the geometry optimization. A Gaussian smearing of 0.05 eV and 1 × 2 × 1 gamma-centered Monkhorst–Pack were used for the geometry optimization. Geometry-optimized GB structures with 8-4 and 7-5 periodic ring motifs were built, which were consistent with our experimental ADF-STEM observations and previously reported works[7,8] (Supplementary Fig. 1).

The formation energy ($E_{formation}$) of the GB ring structure was calculated based on its definition:

$$E_{\mathrm{formation}} = \frac{E_{\mathrm{ring}} - n_{\mathrm{Mo}} \times E_{\mathrm{MoS_2}} - (n_{\mathrm{S}} - 2n_{\mathrm{Mo}}) \times \mu_{\mathrm{S}}}{L} \quad \text{(S6)}$$

where E_{ring} is the electronic energy of the whole system containing the GB ring structures; n_{Mo} is the number of molybdenum atoms in the system; $E_{\mathrm{MoS_2}}$ is the electronic energy of monolayer MoS_2 per formula; n_S is the number of sulfur atoms in the system; μ_S is the

chemical potential per sulfur atom in the ring structures; and *L* is the length of the minor twin GB in the practical first-principle calculations. μ_S was decided within a reasonable range of –5.44 to –4.24 eV. The value –5.44 eV corresponds to the sulfur-poor situation, and it is obtained through $\left(E_{MoS_2} - \mu_{Mo}\right)/2$, where μ_{Mo} is the chemical potential per molybdenum atom in its pure form. The value –4.24 eV corresponds to the sulfur-rich situation, which is equivalent to the chemical potential per sulfur atom in the S_8 molecules under the gas phase, called $\mu_S(S_8)$.

MD simulations. The simulation system contained a monolayer C-MoS_2 or R-MoS_2 membrane, pure water on the left side and 1.0 M NaCl solution on the right side with dimensions of L*X* = 3.743 nm, L*Y* = 2.194 nm, and L*Z* = 15.00 nm (L*X*, L*Y*, and L*Z* were the lengths set for *X*, *Y*, and *Z* axes). L*Z* was set to be sufficiently large to eliminate the image effect in the *Z* direction. The ions were randomly distributed on the right side of the solution. The C-MoS_2 membrane with 8-4 ring structures and R-MoS_2 with 7-5 ring structures were built according to the optimized geometry using DFT and was fixed during the simulation. The MD simulations were performed for a canonical ensemble (NVT) with periodic boundaries in all the three dimensions using a time step of 1 fs with Gromacs 5.0 [9]. The temperature was controlled at 300 K using a velocity-rescale thermostat. The Optimized Potentials for Liquid Simulations all-atom force field[10] was used for both MoS_2 and the ions, and the transferable intermolecular potential 3 point model[11] was used for the water molecules. The Lennard–Jones parameters and charge of MoS_2 were adopted from a previous work[12]. The particle mesh Ewald[13] scheme was used to treat the long-range electrostatic interaction with a cutoff set at 1.0 nm, and the same cutoff was used for the van der Waals interactions. To calculate the number of H bonds, a distance cutoff of 3.5 Å between the donor and the acceptor and a 30° angle cutoff for the donor–hydrogen–acceptor angle were used. The total simulation time was 100 ns. Based on our ADF-STEM observations, we also constructed a system of monolayer MoS_2 with an irregular pore of 1.3 nm × 1.9 nm and performed the water/ion separation simulations using the same conditions (Supplementary Fig. 11).

Characterizations. The optical microscopy images were recorded using Olympus BX51M. Scanning electron microscopy (SEM) characterization was performed to study the morphology of the MoS_2 films using the FEI Magellan 400 microscope with a voltage of 3 kV. The Raman and photoluminescence (PL) spectra were collected using a Witec alpha300 confocal Raman microscope equipped with a RayShield Coupler and a 532 nm solid-state laser. An excitation light with a power of 2.5 mW was focused onto the samples. The AFM measurements for analyzing the sample morphology and thickness were carried out under the tapping mode using Bruker Dimension ICON. Commercial silicon tips (RTESPA-150-30, Bruker) with a radius of 31 nm and spring constant of 2.720 N/m were used for the force-indentation experiments. Atomic-resolution ADF-STEM imaging was performed with a Thermo Fisher Titan Themis Z transmission electron microscope equipped with a double Cs (spherical

aberration) corrector, a high-brightness electron gun (x-FEG), and an electron beam monochromator. To reduce the electron-beam-induced damage, we operated the microscope at an acceleration voltage of 80 kV with a column (at the sample) vacuum of approximately 2–4 × 10^{-7} Torr at room temperature. Gauss high-pass (to reduce contamination effects) and low-pass (to reduce scanning noise) filtering were used to enhance the contrast of the images. The cross-sectional STEM samples were prepared using a Helios NanoLab 660 DualBeam FIB system.

Supplementary Figures

7-MR (4 Mo, 3 S)

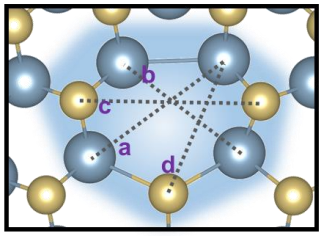

No.	Atom-to-atom distance, D' (Å)	Accessible distance, D_A (Å)
a	5.5	2.0
b	5.2	1.7
c	6.5	2.9
d	4.9	1.4
Pore geometry		2.9 × 1.4 Å

7-MR (3 Mo, 4 S)

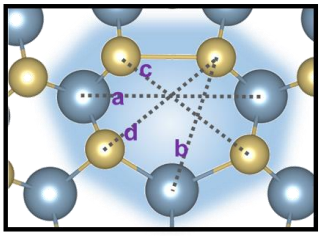

No.	Atom-to-atom distance, D' (Å)	Accessible distance, D_A (Å)
a	6.5	3.0
b	5.1	1.6
c	5.5	1.9
d	5.1	1.5
Pore geometry		3.0 × 1.5 Å

8-MR

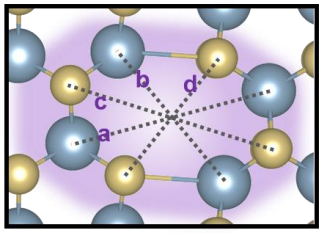

No.	Atom-to-atom distance, D' (Å)	Accessible distance, D_A (Å)
a	7.5	4.0
b	6.1	2.6
c	7.8	4.2
d	6.0	2.4
Pore geometry		4.2 × 2.4 Å

Supplementary Figure 1. DFT-optimized 7-MR and 8-MR structures. Distance available for transport (D_A) can be approximately calculated as: $D_A \approx D' - r_a - r_b$, where D' is the atom-to-atom distance, and r_a and r_b are the van der Waals radii of individual atoms, which are 1.76 and 1.8 Å for Mo and S, respectively[14].

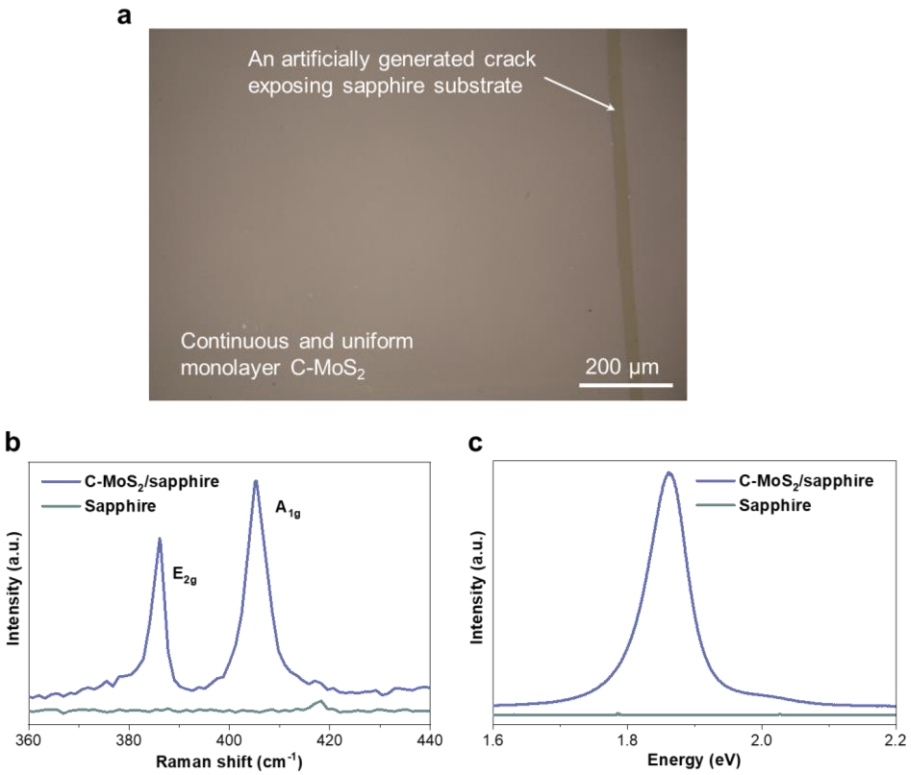

Supplementary Figure 2. Characterization of C-MoS_2 grown on a sapphire substrate. a, Optical microscopy image showing a continuous and uniform film with an artificially generated crack exposing the underlying sapphire substrate. **b and c,** Raman and PL spectra of C-MoS_2/sapphire, respectively. Raman peaks of E_{2g} and A_{1g} are at 385.6 and 406.1 cm^{-1}, respectively. The PL peak of the A exciton is at 1.861 eV with a full width at half maximum of ~0.06 eV. All these features are in good agreement with those reported in previous reports on high-quality monolayer MoS_2[15,16].

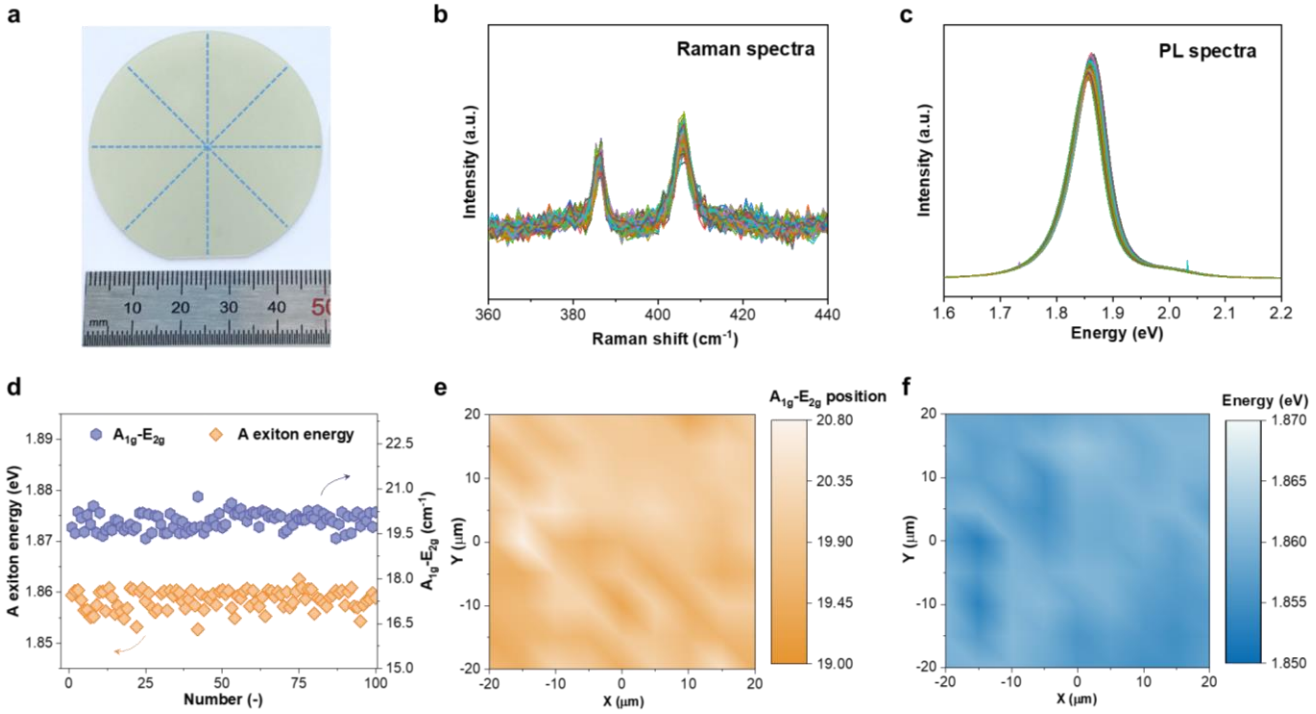

Supplementary Figure 3. Raman and PL characterization of the wafer-scale C-MoS_2 film. a, Digital photograph of a C-MoS_2 film grown on a 2-inch-diameter sapphire wafer. **b and c,** Overlaid Raman and PL spectra acquired from 100 different positions on the four lines shown in **a**, respectively. All the Raman and Pl spectra are nearly identical with the same peak position. **d,** Statistical value of the peak position difference of A_{1g} and E_{2g} (left) and the PL peak energy (right) of the two-inch C-MoS_2 film as functions of the point position. **e** and **f,** 40 μm × 40 μm mapping of the A_{1g} – E_{2g} position and A exciton peak position, respectively. The value of A exciton peak position varies from 1.853 to 1.863 eV, and the A_{1g} – E_{2g} position value ranges from 19.45 to 20.74 cm^{-1}. These data demonstrate the uniformity of the prepared monolayer MoS_2 film at the wafer scale.

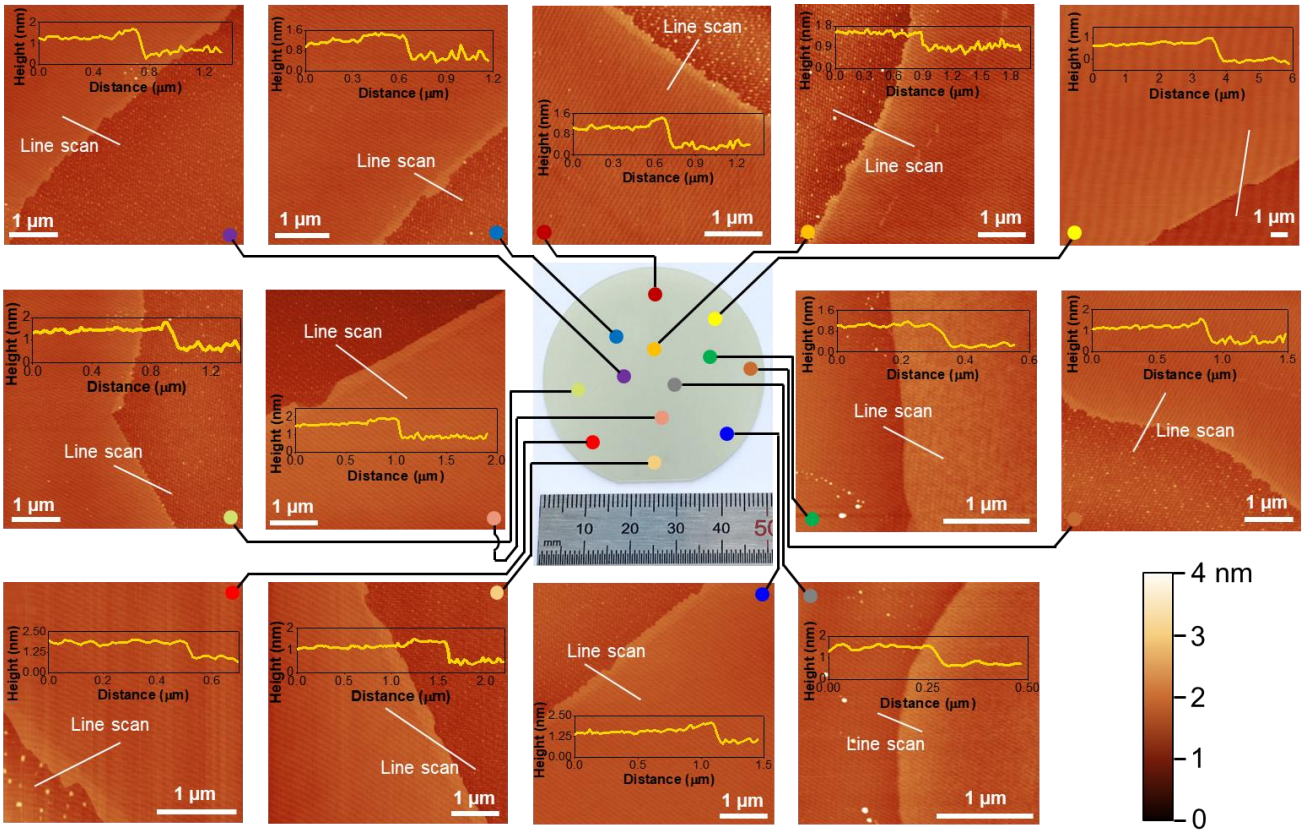

Supplementary Figure 4. AFM images of the C-MoS_2 film grown on a 2-inch-diameter sapphire wafer. The images acquired from different locations show a monolayer morphology. Before the measurements, the wafer was cut into small pieces, and the steps were formed by removing part of the MoS_2 film using PDMS.

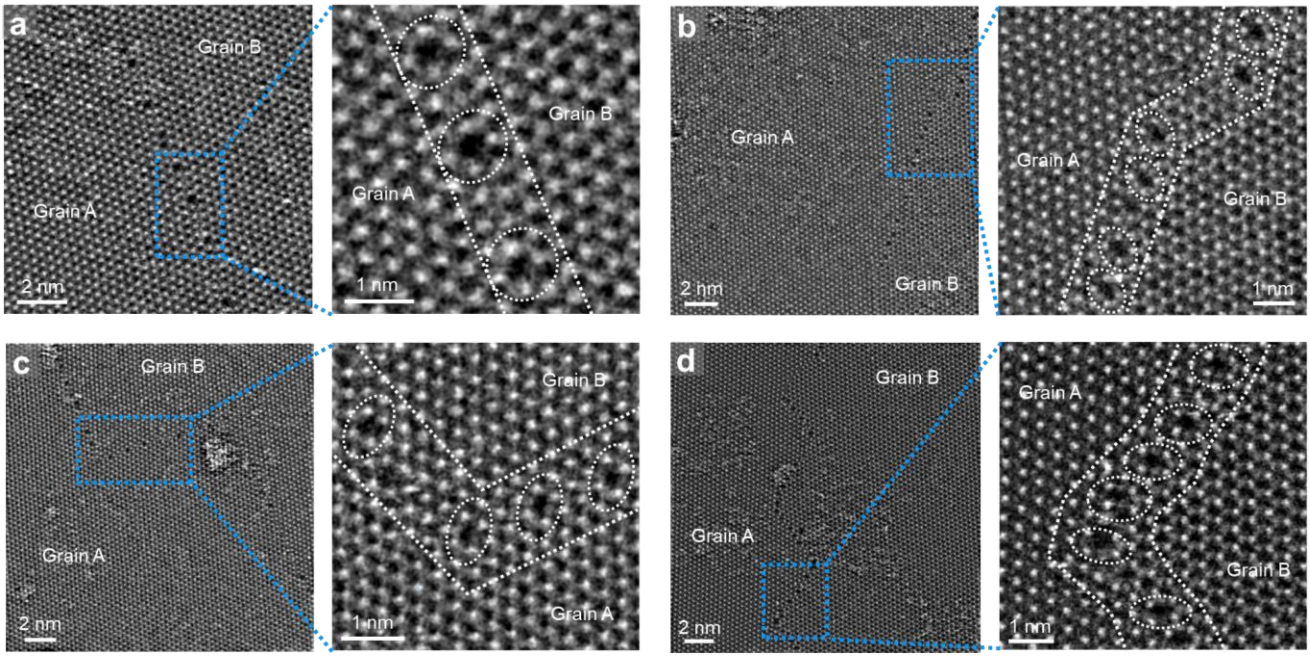

Supplementary Figure 5. Mirror-twin GBs in C-MoS_2. a–d, ADF-STEM images acquired from different locations of a C-MoS_2 film, showing boundaries formed between two interconnected grains with a 60° orientation relationship. In the magnified images (right panels), the dashed lines and circles outline the GB and 8-MR pores, respectively.

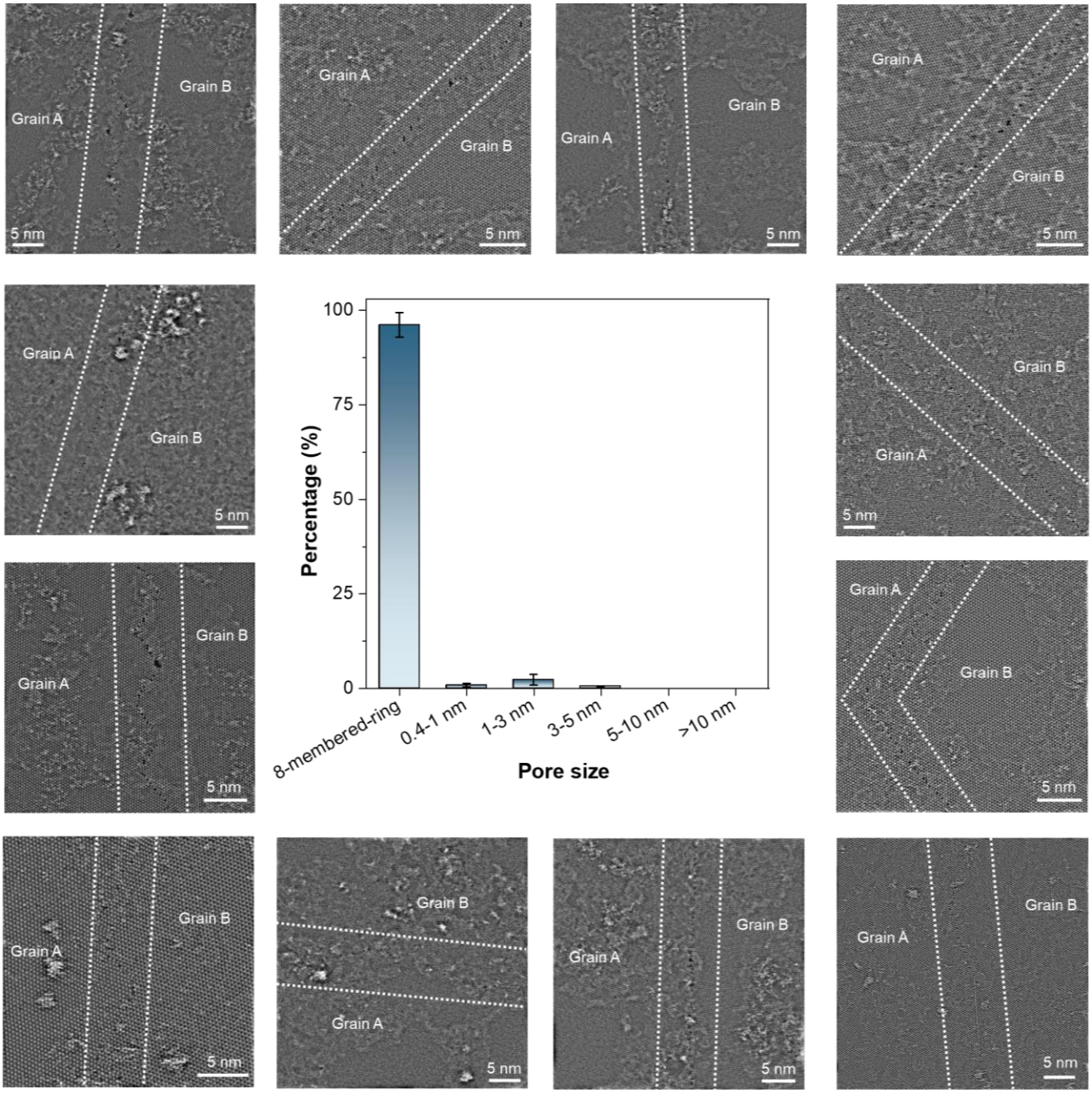

Supplementary Figure 6. Statistics of the pores at the C-MoS_2 GBs based on the ADF-STEM images. In each ADF-STEM image, the dashed lines outline the GBs. Some cloud-like substances observed on monolayer MoS_2 are polymer residues introduced during the transfer process.

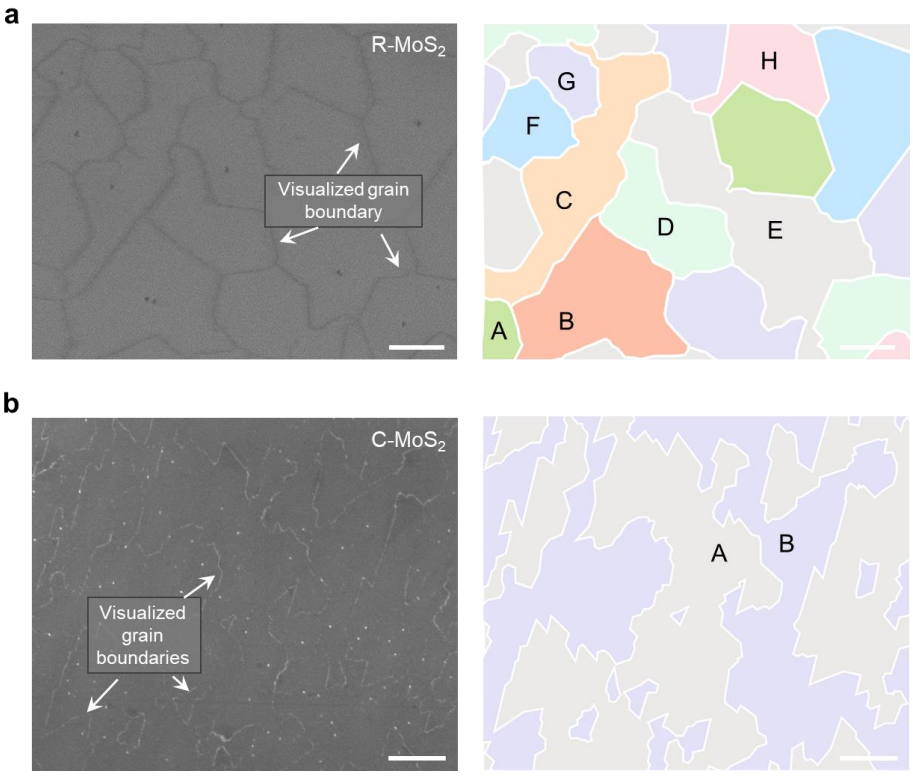

Supplementary Figure 7. Visualization of the MoS_2 GBs. a and **b**, SEM images of the R-MoS_2 (**a**) and C-MoS_2 (**b**) films grown under standard conditions (left panels); the identified GBs are delineated to show the grain connectivity (right panels). Scale bars, 2 μm. Prior to the imaging, the films were heated in humid air to accumulate contaminants at the GBs, making them easily identifiable by SEM. The average grain sizes were determined to be ~7.4 and ~6.8 μm^2 for R-MoS_2 and C-MoS_2, respectively (see Supplementary Note 1 for detail).

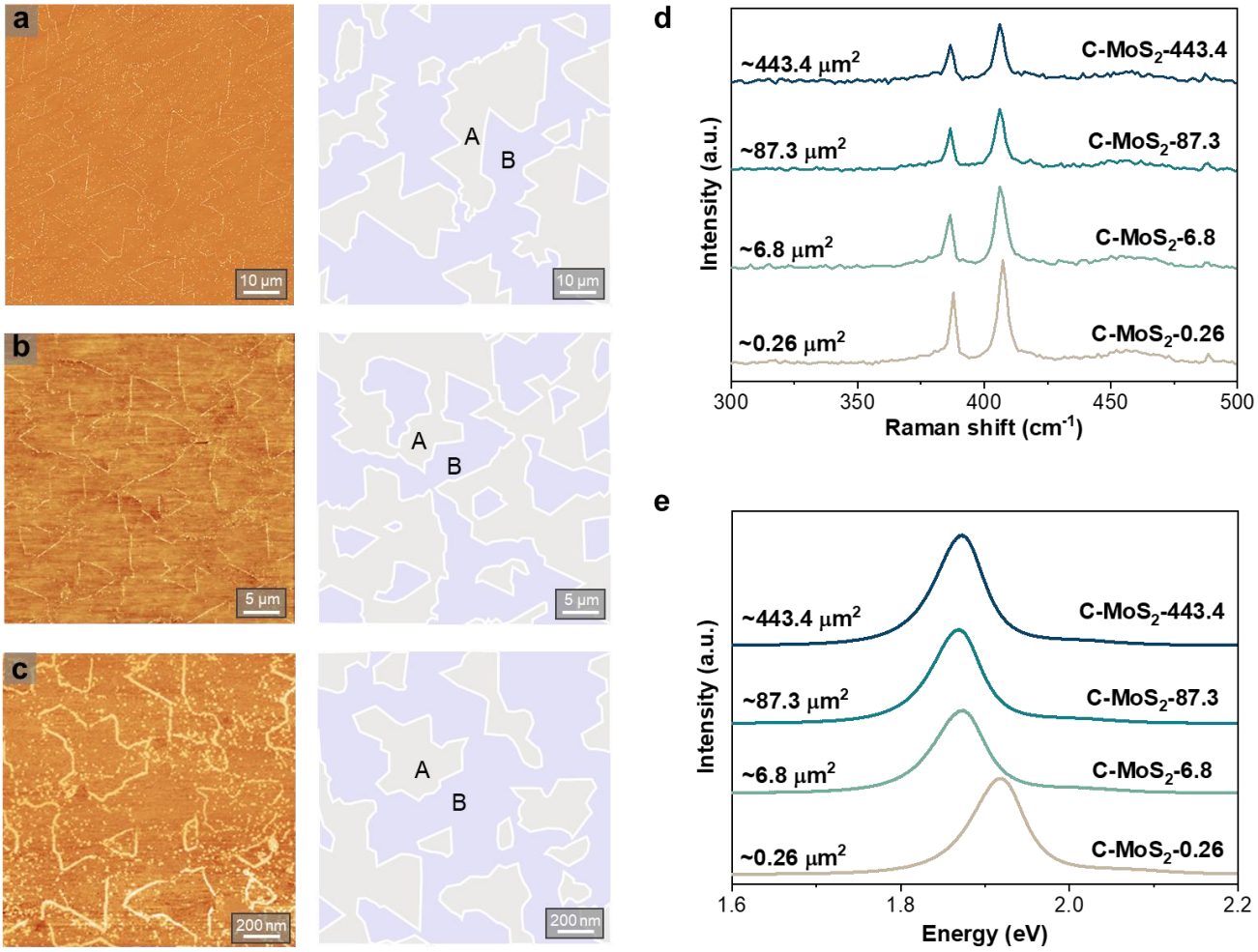

Supplementary Figure 8. Tuning the C-MoS_2 grain size. a–c, AFM topographic images of the C-MoS_2-443.4 (**a**), C-MoS_2-87.3 (**b**), and C-MoS_2-0.26 (**c**) films (left panels); the identified GBs are delineated to show the grain connectivity (right panels). **d,** Raman and **e,** PL spectra of C-MoS_2 with different grain sizes, obtained by integrating the collected spectra over an area of 300 × 300 μm. C-MoS_2-0.26 exhibits a blue shifted PL peak relative to those of the other samples due to the local change of strain around the GBs[17-19].

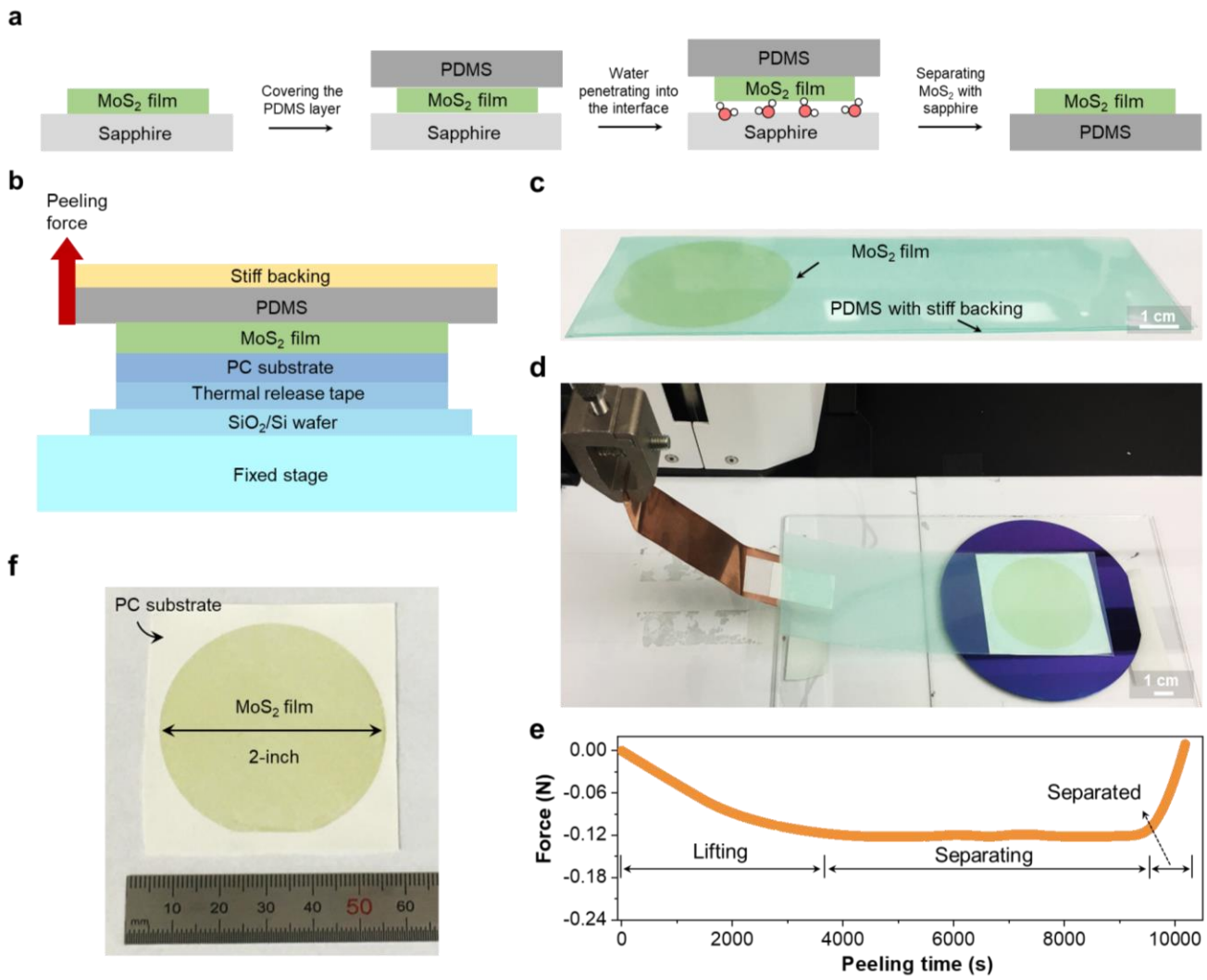

Supplementary Figure 9. Controlled transfer of a wafer-scale MoS_2 film to a porous PC substrate. **a,** Schematic of the water-assisted detachment of MoS_2 from sapphire. **b,** Schematic of the PDMS-assisted transfer process. **c and d,** Photographs of a MoS_2 film on the PDMS strip and the controlled peeling of the PDMS layer from the PC substrate by a motorized machine at a constant speed of 0.5 μm s^{-1}. **e,** Measured peeling force during the transfer process. **f,** Photograph of the prepared MoS_2 membrane (monolayer MoS_2 film supported on a PC substrate).

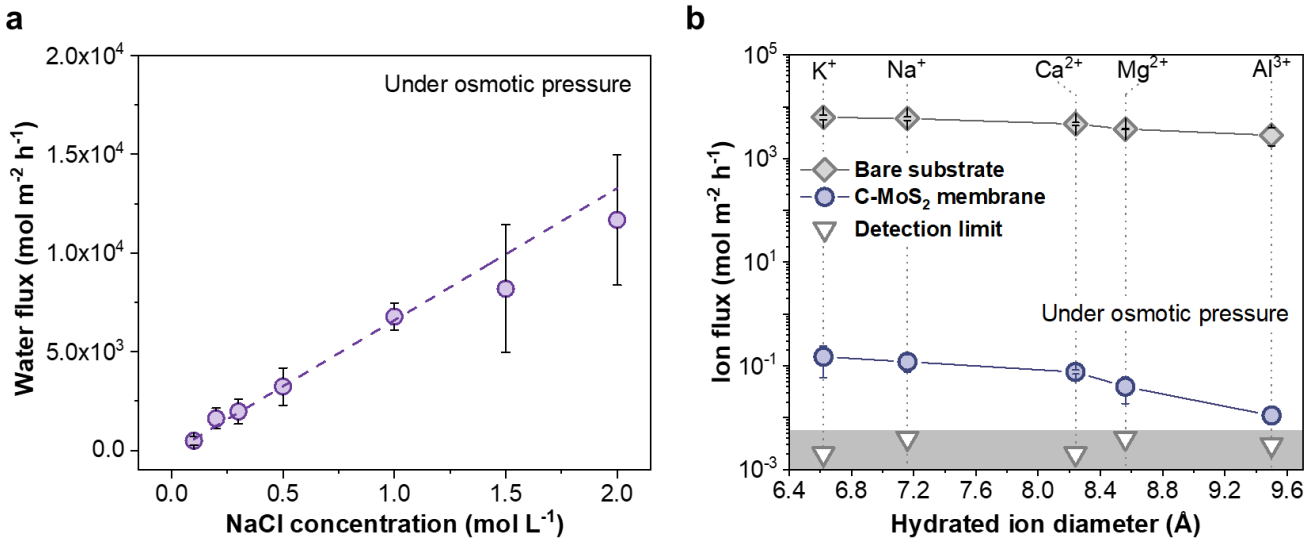

Supplementary Figure 10. Water and ion transport behaviors of the C-MoS_2-6.8 membrane. a, Water flux as a function of NaCl concentration. Feed side: DI water; draw side: NaCl solution. **b,** Fluxes of ions with different hydrated diameters. Feed side: 0.1 M salt solution (KCl, NaCl, $CaCl_2$, $MgCl_2$ or $AlCl_3$); draw side: 2 M sucrose solution. Error bars denote the standard deviations from three different samples.

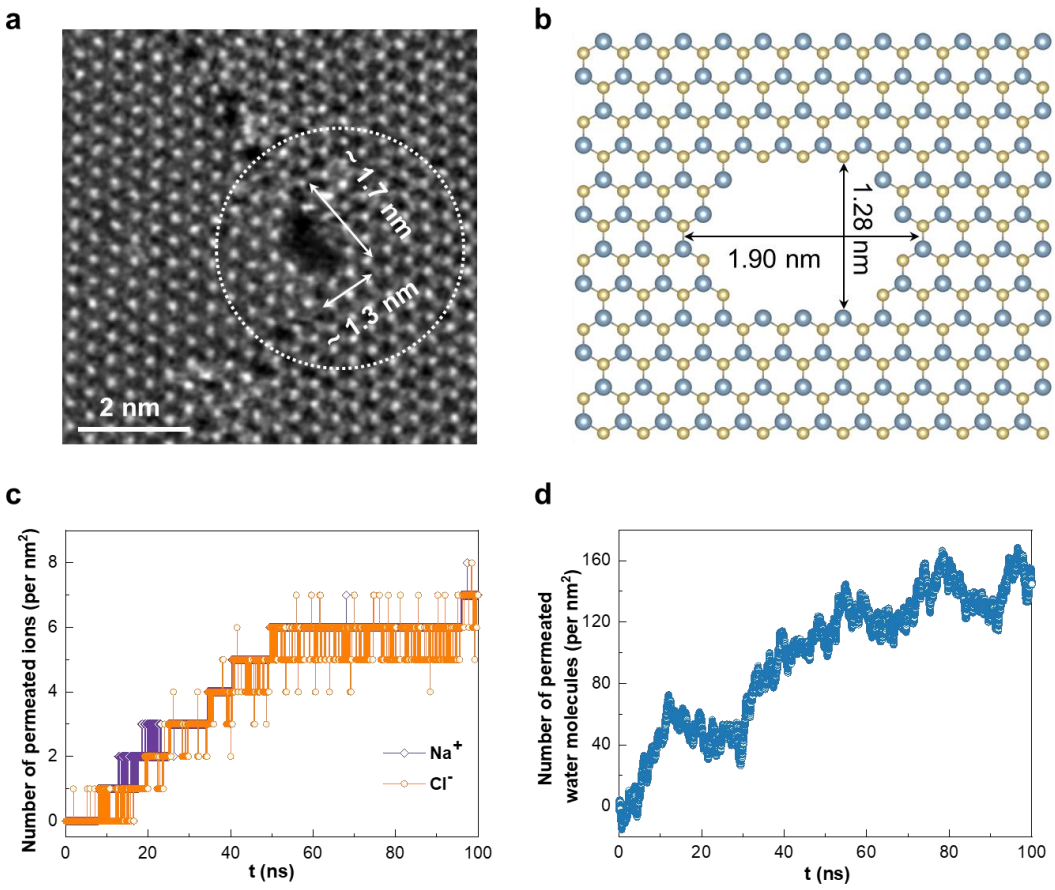

Supplementary Figure 11. An irregular large pore occasionally observed at the C-MoS_2 GB. a, ADF-STEM image showing an irregular pore larger than 1 nm. **b**, Structural model constructed based on the image in (**a**) for MD simulations. **c** and **d**, MD simulation results, revealing that such a large pore is permeable to (**c**) Na^+ and Cl^- ions as well as (**d**) water molecules.

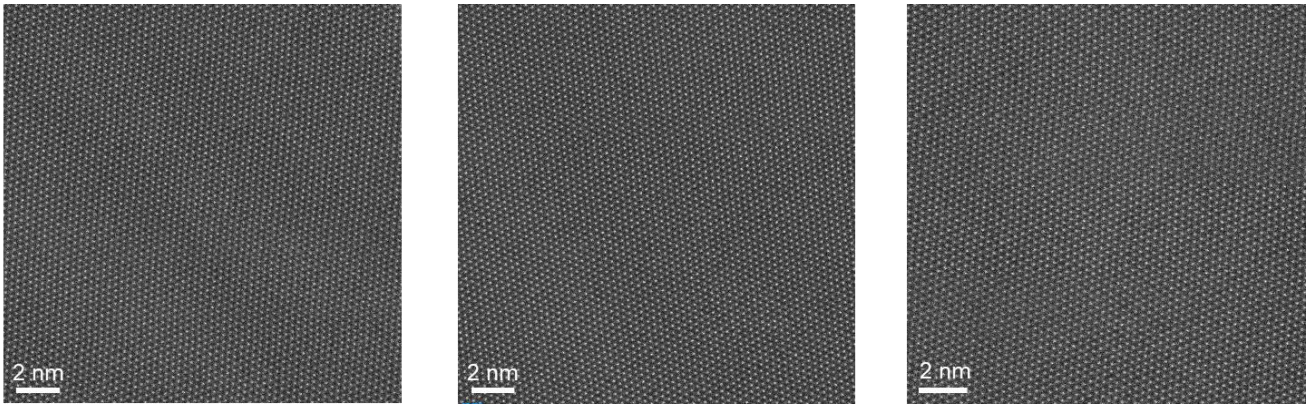

Supplementary Figure 12. Bulk region of monolayer C-MoS_2. ADF-STEM images acquired from the bulk region of the C-MoS_2-6.8 film, confirming the absence of structural defects outside GBs.

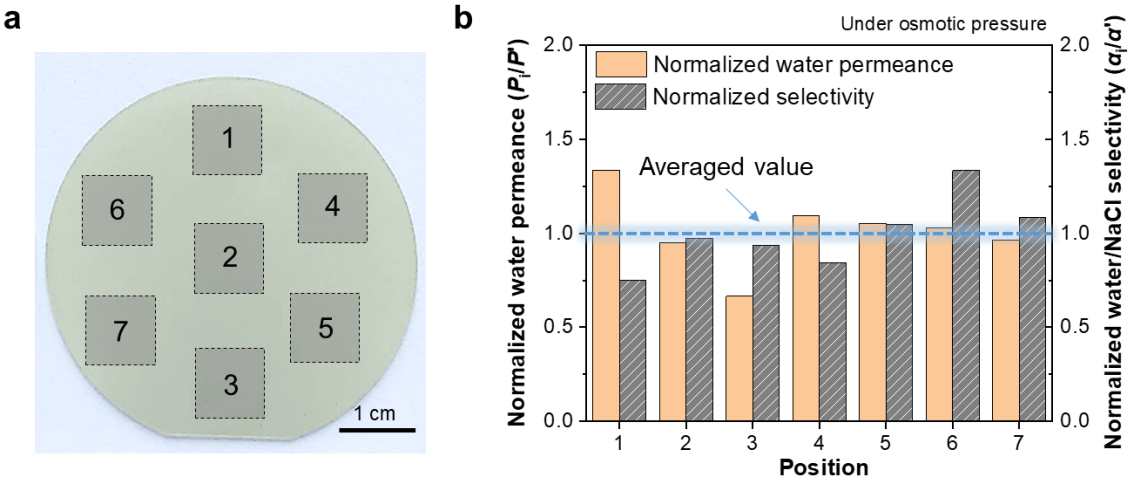

Supplementary Figure 13. Structural homogeneity of monolayer MoS_2. a, Photograph of a C-MoS_2-0.26 film grown on a 2-inch sapphire wafer. The numbered regions are where seven membranes were fabricated. **b**, Normalized water permeance and water/NaCl selectivity of the seven C-MoS_2 membranes. P_i and P' indicate the water permeance of a MoS_2 membrane at a specific region and the average water permeance, respectively. α_i and α' represent the selectivity of a MoS_2 membrane at a specific region and the average selectivity, respectively. Feed side: 0.1 M NaCl solution; draw side: 2 M sucrose solution.

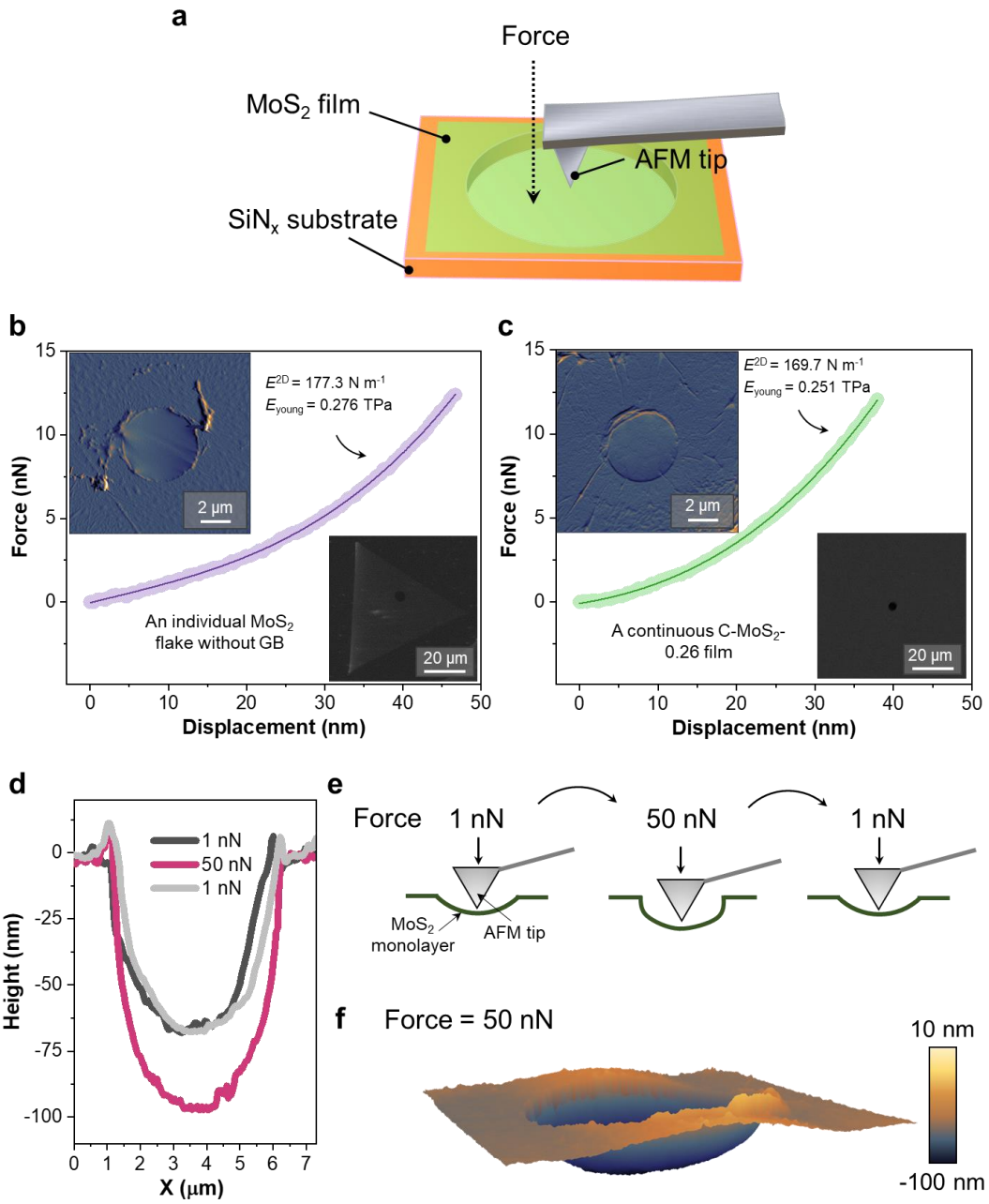

Supplementary Figure 14. AFM-measured mechanical property. a, Schematic of the AFM indentation measurement. Force–displacement curves of **b**, an individual MoS_2 flake without GB and **c,** a continuous C-MoS_2-0.26 monolayer. Difference of the Young's modulus is within ~5%, indicating that the mechanical properties of MoS_2 are well-maintained. Young's modulus of our C-MoS_2-0.26 membrane (0.215 TPa) is nearly three orders of magnitude higher than that of commercial polyamides[20]. AFM (upper left corner) and SEM (bottom right corner) images are inserted in both the figures. **d**, Changes in the AFM topological profiles of the C-MoS_2-0.26 monolayer with applied force on the AFM tip. Initially, a force of 1 nN was applied and then increased to 50 nN, followed by recovering to the initial force of 1 nN. For each applied force, the height across the central line of the probed region

as a function of displacement X was continuously recorded for 1 h. **e**, Schematic of the AFM measurements performed using different forces. **f**, Three-dimensional AFM topological image corresponding to a force of 50 nN. The recovery of the AFM topological profile after the force was reduced from 50 nN to 1 nN indicates that the C-MoS_2-0.26 monolayer with GBs was mechanically robust (withstand a pressure of ~9 MPa considering the contact area of ~5800 nm^2 at an indentation depth of ~100 nm). The GBs with 8-MR structures in the MoS_2 monolayer exhibited an excellent fracture resistance[21] under a fracture stress of at least 1000 MPa[22,23], indicating a sufficient mechanical strength for the membrane-based RO operation.

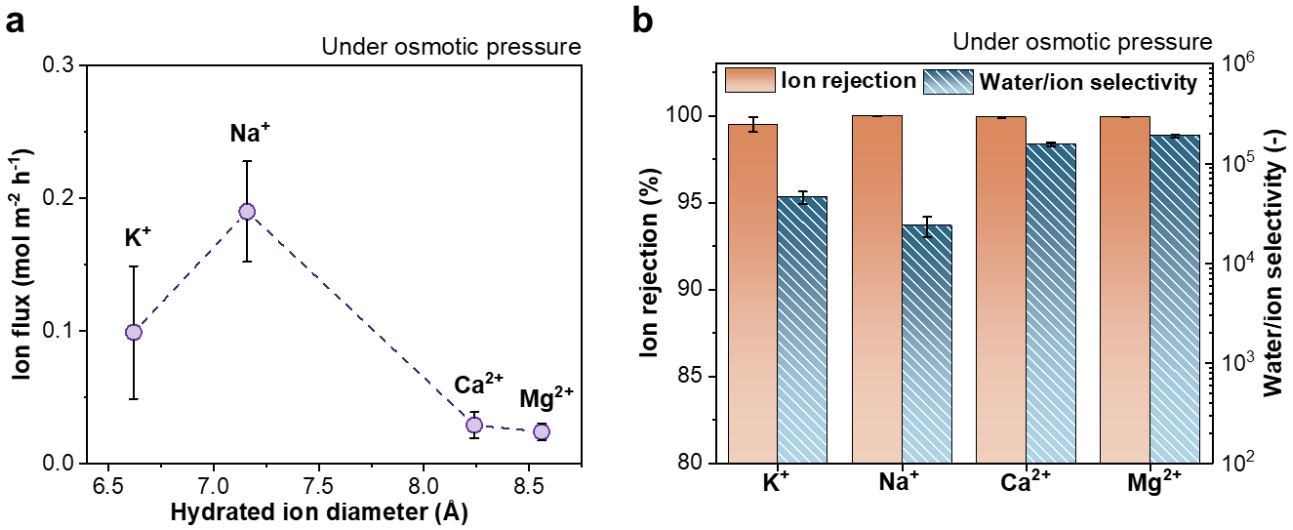

Supplementary Figure 15. Water and ion permeation experiments performed using synthetic seawater and 2 M sucrose as the feed and draw solutions, respectively. a, Ion flux, and **b**, ion rejection and water/ion selectivity of the C-MoS_2-0.26 membranes. The synthetic seawater was a mixture of KCl (0.0093 M), NaCl (0.42 M), Na_2SO_4 (0.029 M), $CaCl_2$ (0.011 M) and $MgCl_2$ (0.056 M). Error bars denote the standard deviations from three independent membrane samples.

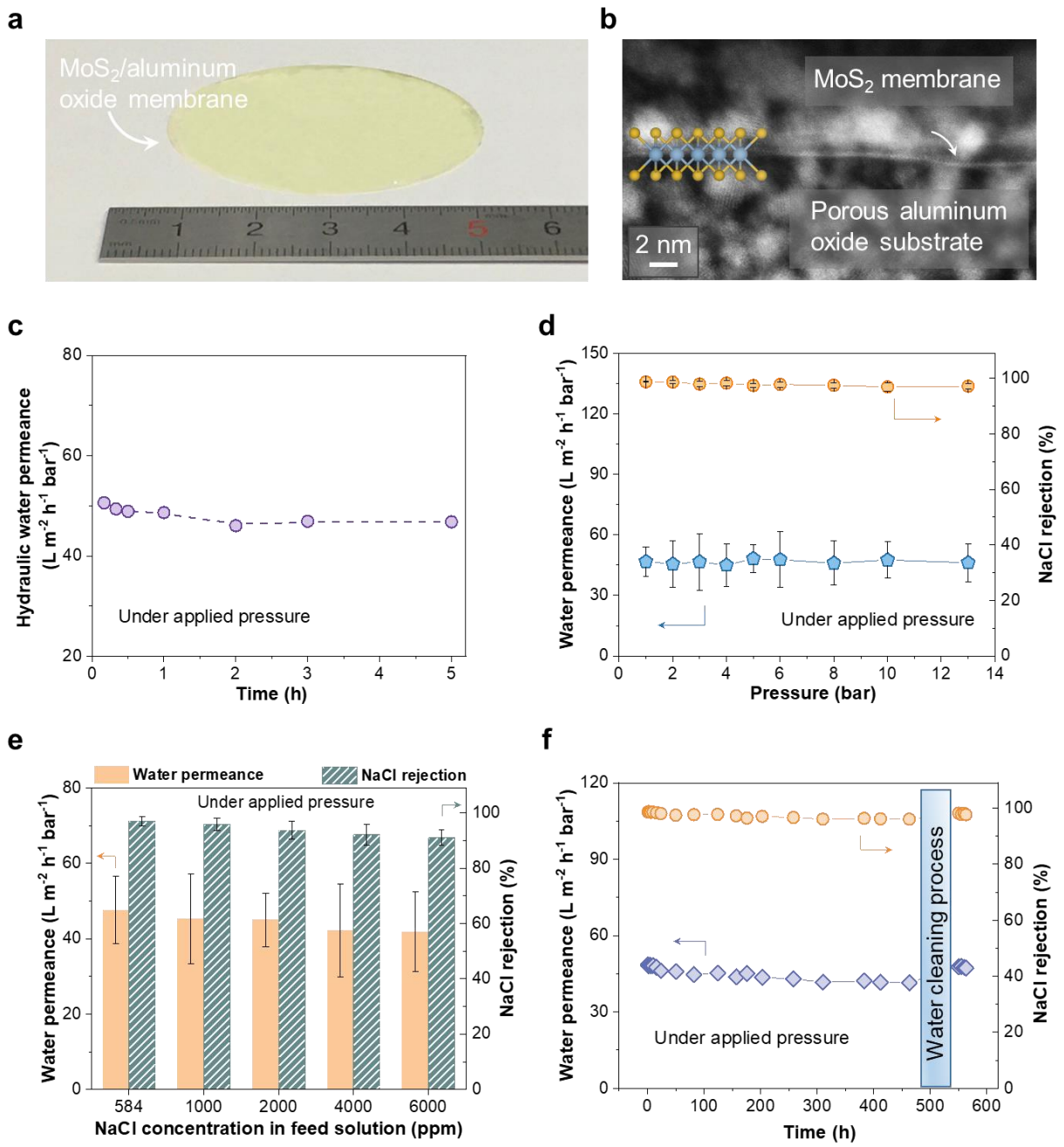

Supplementary Figure 16. Water/ion permeation of C-MoS_2-0.26 measured in RO mode. a, Photograph of the MoS_2 membrane fabricated on an AAO substrate (diameter: ~4 cm). **b,** Cross-sectional STEM image of the membrane, confirming the formation of a monolayer MoS_2 film. **c**, Hydraulic water permeance (pure water permeation), under 2 bar as a function of the operation time. **d**, Effect of operating pressure on the water permeance and NaCl rejection. Feed concentration: 0.01 M. Higher pressure (> 13 bar) operation was not performed due to the failure of the AAO support used in the current study. **e**, Effect of NaCl concentration in the feed solution on the water permeance and NaCl rejection under an applied pressure of 10 bar. Error bars denote the standard deviations from

three different samples. **f**, Long-term continuous water/NaCl separation results (feed solution: 0.01 M NaCl, applied pressure: 4 bar, pH = 7, T = 25 °C, dead-end operation).
Note: The slight decrease of water permeance from 48 h can be attributed to the concentration polarization effect. After a simple cleaning step (filtration of pure water at 4 bar after cleaning with pure water), the initial values of the water flux and salt rejection were recovered. This result demonstrated the structural stability of the MoS_2 membrane over a long period of operation under the RO configurations.

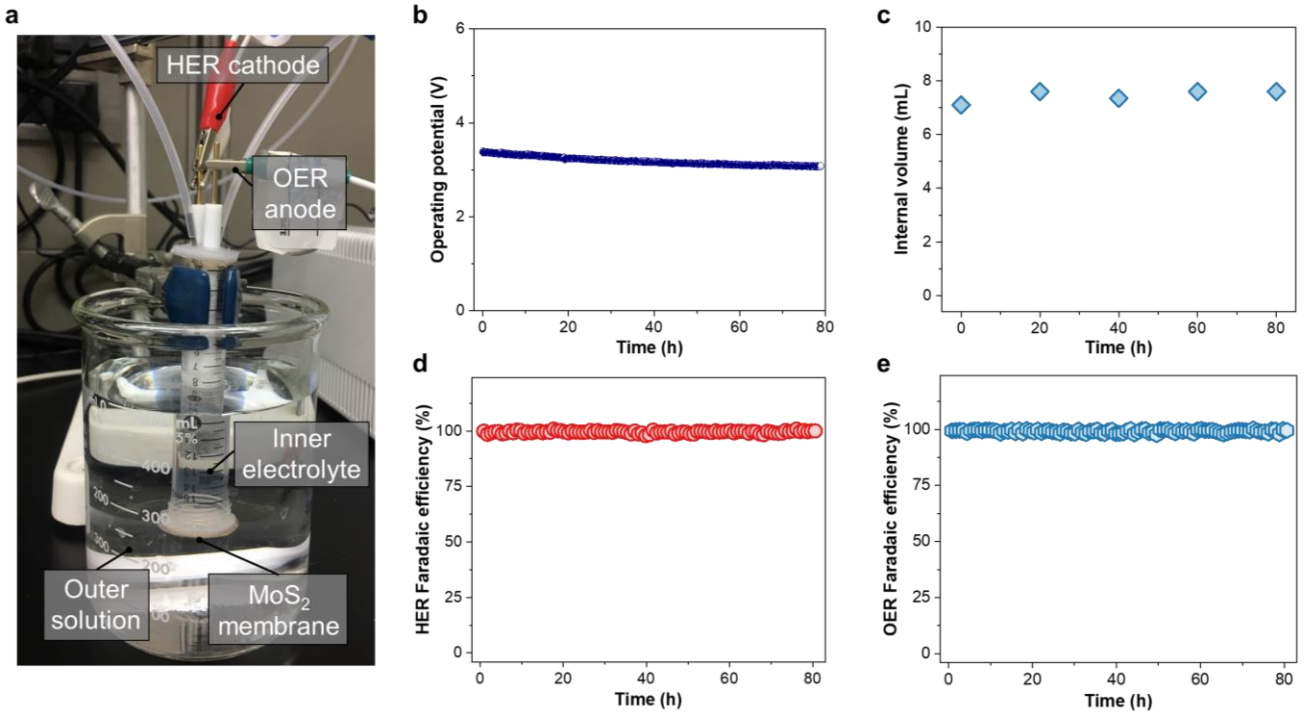

Supplementary Figure 17. Electrolysis of saline water using the C-MoS_2-0.26 membrane. a, photograph of the electrochemical cell used for the electrolysis of saline water. **b,** Chronopotentiometry measurements conducted at 76 mA with a 0.8 M NaH_2PO_4 inner electrolyte solution and a 0.6 M NaCl outer solution as the saline water source. The operation potential stabilized at around 3.15 V after 80 h. **c**, Change in the internal volume over 80 h of operation. The maintained internal volume indicates the balance between the influx of water into the cell and the water consumed during the electrochemical water splitting. **d** and **e**, HER and OER Faradaic efficiencies over 80 h of operation.

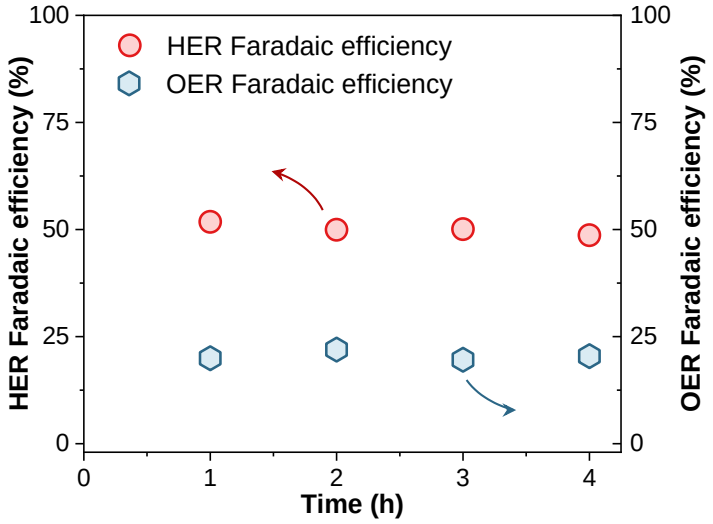

Supplementary Figure 18. Electrolysis of saline water (0.6 M NaCl) without using a separation membrane. The Faradaic efficiencies for HER and OER over 4 h of operation. The electrochemical experiments were conducted using Pt electrodes as anode and cathode in a single-compartment electrochemical cell operated at 76 mA.

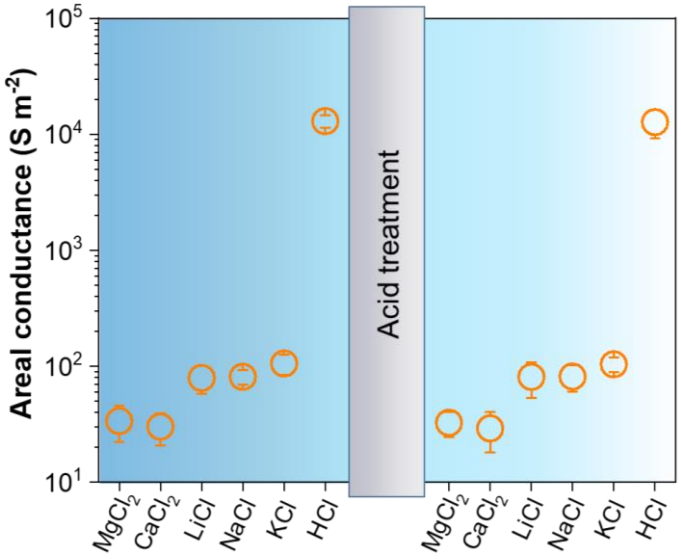

Supplementary Figure 19. Evaluation of the acid resistance of C-MoS_2-0.26. Ionic conductance of the C-MoS_2-0.26 membranes (supported on SiN_x/Si substrates) measured before and after treatment in 0.1 M HCl for 10 h. After the acid treatment, the membranes were carefully cleaned by DI water and tested again. Error bars denote the standard deviations from three different samples.

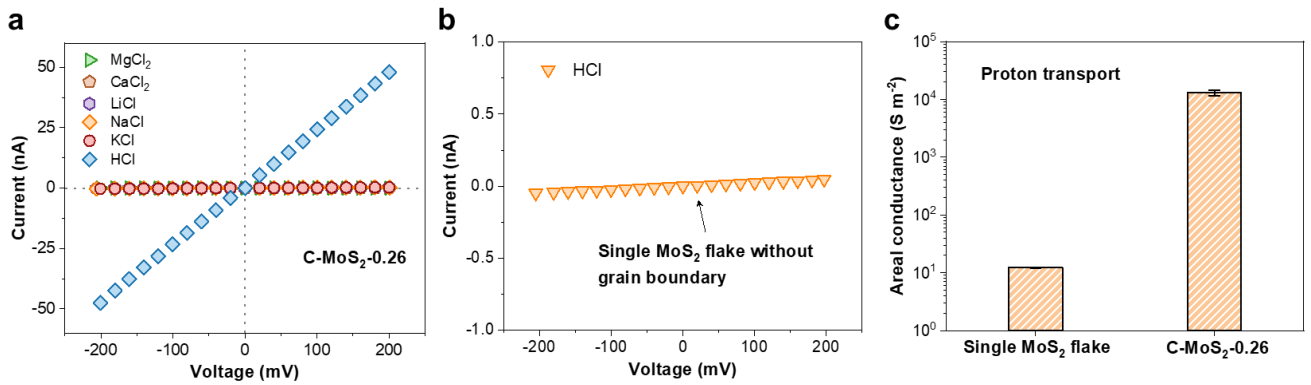

Supplementary Figure 20. Electric-field-driven proton and ion transport. a, *I–V* curves of the C-MoS_2-0.26 membrane for HCl and various salts, including KCl, NaCl, LiCl, $CaCl_2$, and $MgCl_2$. For each measurement, the salt concentration was 0.1 M on both sides of the devices. **b,** *I–V* curve of the membrane fabricated using a single-crystalline MoS_2 flake (without GB). 0.1 mol L^{-1} HCl solution was used. **c,** Comparison of the areal conductance of C-MoS_2-0.26 and the single-crystalline MoS_2 flake. Error bars denote the standard deviations from three different samples.

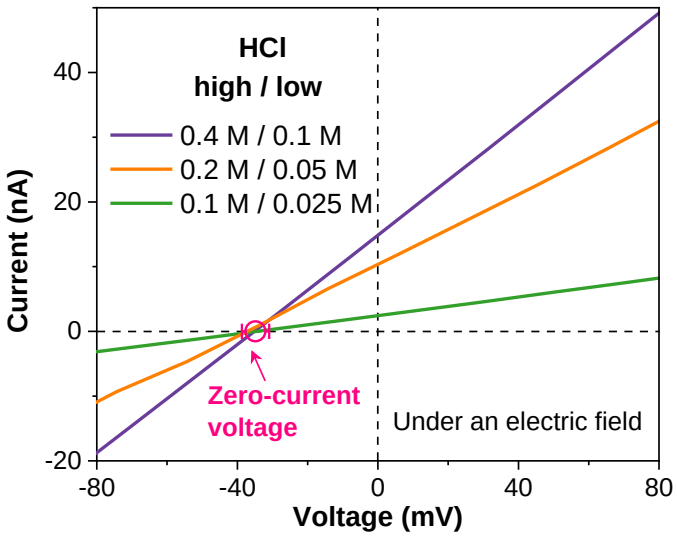

Supplementary Figure 21. *I–V* curves for different concentrations of HCl in the two reservoirs connected by the C-MoS_2-0.26 membrane. The same concentration gradient Δ of four was used for all the measurements. The pink symbol denotes the voltages at zero current. The horizontal bar represents the statistical error in determining V_0 from the measurements obtained from several devices.

Supplementary Table

Supplementary Table 1. Comparison of the water/NaCl separation performances of various membranes driven by osmotic pressure.

Membrane	Thickness	Osmotic pressure, $\Delta\pi$ (bar)	Na^+ flux, J_s (mol m^{-2} h^{-1})	Water flux, J_w (mol m^{-2} h^{-1})	Water permeance (mol m^{-2} h^{-1} bar^{-1})	Selectivity (J_w/J_s)	Ref.
Physically confined GO	5 μm	~70	0.05	27.8	0.37	555.6	[24]
KCl-controlled GO	280 nm	~12	4.8×10^{-3}	20	1.67	4170	[25]
Amine-functionalized GO	200 nm	~24.5	6.1×10^{-3}	30.83	1.26	5040	[26]
Reduced GO	100 nm	~19.8	0.2	216	10.9	1080	[27]
Pristine MoS_2	~4 μm	~48	0.86	5.86	0.12	6.8	[28]
Peptide modified porous MoS_2	~1 μm	~28	0.04	277.7	9.92	7553.4	[29]
Covalently functionalized MoS_2	500 nm	~148	4.8×10^{-4}	205.6	1.39	3571	[30]
CVD graphene	~4 nm	~22.6	180.5	2400	106.4	13.3	[1]
CVD graphene/CNT network	~50 nm	~12.5	5.0	6944	555.5	1388	[31]
ODPA functionalized CNT	~2 μm	~37.2	0.27	1805	48.5	6685.2	[32]
Pristine MXene	~400 nm	~4.9	0.22	23.2	4.74	104.5	[33]
Thermally-treated MXene	~526 nm	~9.9	0.012	32.7	3.33	2722.5	[33]
Al^{3+} intercalated MXene	1.1 μm	~44.6	0.19	50.4	1.13	271.6	[34]
Conjugated polymer framework	~8 nm	~44.6	0.73	5004	112.2	6854	[4]
2D aluminum-based MOF	20 nm	~36	0.0016	80.03	2.22	5×10^4	[35]
UiO-66-GO	~500 nm	~49.6	0.12	1417.8	28.5	1.1×10^4	[36]
Polyamide-UiO-66 TFN	603 nm	~96.1	0.08	1150	11.9	1.4×10^4	[37]
Polyamide-NaY zeolite TFN	~2 μm	~49.6	0.17	916	18.5	5392	[38]
Polysulfone-LDH-GO TFN	-	~49.6	0.11	744	15	6763.6	[39]
Commercial polyamide TFC	~1 μm	~49.6	0.07	866.7	17.5	1.2×10^4	[40]
Commercial CTA	~100 μm	~19.8	4.17	1203.7	60.8	288.9	[27]
C-MoS_2-0.26	~0.7 nm	~44.6	0.16	10347.2	232	6.5×10^4	This work

GO, graphene oxide; rGO, reduced graphene oxide; CTA: cellulose triacetate; TFC: thin-film composite; TFN: thin-film nanocomposite; ODPA: Octadecylphosphonic acid; LDH: layered double hydroxides.

Supplementary Table 2. Comparison of the water/NaCl separation performances of various membranes driven by applied pressure.

Membrane	Thickness	Applied pressure (bar)	NaCl concentration in feed solution (ppm)	Water permeance in NaCl-water system (L m^{-2} h^{-1} bar^{-1})	Pure water permeance (L m^{-2} h^{-1} bar^{-1})	Salt rejection (%)	Ref.
GO	-	3.4	1170	-	27.6	19	[41]
rGO	53 nm	5	1170	-	3.3	42	[42]
GO-CNTs	~100 nm	5	584.4	5.5	-	59	[43]
GO-graphene	~30 nm	~50	2000	0.47	-	85	[44]
ZIF-8@f-GO	~105 nm	1	1000	49.8	-	30.3	[45]
CVD graphene-CNTs	~50 nm	5	2000	97.6	110.6	86.3	[31]
Covalent functionalized MoS_2	500 nm	9	5844	6.7	-	77.9	[30]
MFI-type zeolite	~2 μm	20.7	5844	0.005	-	76	[46]
UiO-66	~2 μm	10	2000	0.14	-	50	[47]
TpPa-COF	~200 nm	5	1000	60		49.2	[48]
$TpTG_{Cl}$-COF	~2 μm	4	1000	42	-	23	[49]
Turing-type polyamide membrane	~20 nm	4.8	2000	12.5	-	51.2	[50]
Conjugated polymer framework	~24 nm	4	584.4	9.3	9.5	83	[4]
Commercial Dow Filmtec NF270	-	1	1000	10	-	35.6	[45]
Commercial SW30	-	20	2000	0.7	-	93.8	[51]
Commercial polyamide TFC (blue diamond)	-	20	2000	1.0		74	[52]
Commercial GE AG	-	20	2000	2.45	-	90.2	[51]
Commercial Sepro NF 2A	-	10	2000	-	10.1	24.8	[53]
Commercial Synder NFW	-	8.3	2000	-	5.4	20	[54]
Commercial Synder NFX	-	8.3	2000	-	2.4	40	[54]
Aromatic polyamide MPD-Trip20	339 nm	15.5	2000	9.2	-	95.5	[55]
C-MoS_2-0.26	~0.7 nm	2	584.4	46.8	48.9	97	This work
C-MoS_2-0.26	~0.7 nm	10	584.4	46.1	-	96.8	This work
C-MoS_2-0.26	~0.7 nm	10	2000	45	-	93.7	This work

ZIF-8@f-GO: ZIF-8-nanocrystal-hybridized frozen GO membrane; MPD: m-phenylene diamine; Trip: bridged-bicyclic triptycene-based tetra-acyl chloride; Tp: 1,3,5-triformylphloroglucinol Pa: p-phenylenediamine; Tp: 1,3,5-triformylphloroglucinol; TG_{Cl}: triaminoguanidinium chloride.

Supplementary Table 3. Quantification of the continuous electrochemical water splitting performance.

Time (h)	OER Faradaic efficiency (%)	HER Faradaic efficiency (%)	$[PO_4^{3-}]$ (mmol L^{-1}) in outer solution	$[Cl^-]$ (mmol L^{-1}) in inner electrolyte	$[HClO^-]$ or $[ClO^-]$ (mmol L^{-1}) in inner electrolyte
0	~100	~100	0	0.402	0.003
40	~100	~100	0.026	2.479	0.007
80	~100	~100	0.063	1.425	0.031

Supplementary Table 4. Comparison of the selectivity of proton over other ions with selected artificial proton channels.

Artificial proton channels		Proton areal conductance (S m^{-2})	H^+/M^+ selectivity ("M" indicates alkali metal ions)	Ref.
Amphiphilic peptide channel	H_2N-(Leu-Ser-Ser-Leu-Leu-Ser-Leu)$_3$-$CONH_2$	~6.4×10^6	H^+/Li^+: ~5.6 H^+/Na^+: ~5.0 H^+/K^+: ~4.2	[56]
Functional nonpeptide channel	Rigid rod-shaped polyols	-	$H^+ > K^+ > Na^+ \approx Li^+$	[57]
Peptide nanotube channel	Polytheonamide B	~5.6×10^8	H^+/Cs^+: ~40.0	[58]
Amine-functionalized MOF channel	UiO-66-NH_2	~4×10^3	H^+/Li^+: ~6	[59]
Sulfonated MOF channel	UiO-66@SAG	~5.3×10^2	H^+/Li^+: ~12 H^+/Na^+: ~11.5 H^+/K^+: ~10	[59]
Sulfonated MOF channel	UiO-66-NH-SAG	~1.4×10^3	H^+/Li^+: ~28 H^+/Na^+: ~25 H^+/K^+: ~12	[59]
Sulfonated MOF channel	UiO-66-(NH-SAG)$_2$	~2.1×10^3	H^+/Li^+: ~100 H^+/Na^+: ~80 H^+/K^+: ~74	[59]
C-MoS_2-0.26	Monolayer MoS_2 membrane with angstrom sized 8-MR pores	~1.3×10^4	H^+/Li^+: 170.1 H^+/Na^+: 162.4 H^+/K^+: 126.8 H^+/Mg^{2+}: 416.4 H^+/Ca^{2+}: 460.3	This work

SAG: sulfonic acid groups.

Supplementary Notes

Supplementary Note 1. Estimation of the grain size, GB length, and density of the 8-MR of C-MoS_2 films

The average grain size (A_{grain}) was estimated using the ImageJ software by delineating the MoS_2 GBs shown in the SEM or AFM images followed by calculating the average grain area[60]. Subsequently, the GB length (L_{GB}) was calculated as the length of the side of equilateral triangles with the same area as the MoS_2 grains, using the equation: $L_{GB} = 0.658 \times A_{grain}^{1/2}$. At least three samples were used for the calculations. The density of the 8-MR φ (per cm^2) can be calculated as: $\varphi = 1.5 \times n / A_{grain}$, where n is the number of the 8-MR pores along a GB and was estimated based on our ADF-STEM observations.

Supplementary Note 2. Analysis of AFM force-indentation curves

The AFM indentation test were conducted using a previously established method[61], in which the tip was moved downward, while the cantilever bending and *z*-piezo displacement were recorded. The loading force was obtained by multiplying the cantilever bending by the cantilever spring constant, and the deflection of the membrane was deduced by subtracting the cantilever bending from the *z*-piezo displacement. The relationship between the force (F) and the deflection (δ) can be described as follows:

$$F = \delta_0^{2D} \pi \delta + E^{2D} \frac{q^3 \delta^3}{r^2} \quad \text{(S7)}$$

where δ_0^{2D} is the prestress in the membrane, E^{2D} is the two dimensional elastic modulus, and r is the radius of the well[62]. The dimensionless constant q is related to Poisson's ratio v (0.25 for MoS_2 [63]) as $q = 1 / (1.049 - 0.15v - 0.16v^2) = 0.9985$. The first term indicates the prestretched membrane region valid for small loads, while the second term shows a $F \sim \delta^3$ relationship, which dominates at large loads[61,63]. The other effects can be ignored because the radius of the AFM tip (31 nm) is much smaller than the SiN_x hole radius (2500 nm). E^{2D} was obtained by fitting the force-deflection curves, and the effective Young's modulus E_{Young} was calculated by dividing E^{2D} by the membrane thickness. The obtained E_{Young} for monolayer MoS_2 was ~ 0.276 TPa, which is consistent with the reported values[63,64].

Supplementary Note 3. Discussion on hydrogen production from seawater by combining FO and electrochemical water splitting

The cell was filled with 7.1 mL of 0.8 M NaH_2PO_4 as the inner electrolyte solution buffered at pH 7 and was separated from the 0.6 M NaCl outer solution by the MoS_2 membrane. A volume

of ~0.5 L was chosen for the outer solution in order to maintain an approximately same salt concentration, thereby providing a relatively constant osmotic pressure. A continuous water splitting process was induced by balancing the water influx and the water consumed by electrochemical water splitting. The water influx (F_{influx}) can be described by the following equation:

$$F_{influx} = \tau RT \frac{K_w A_m}{l} \Delta C \quad \text{(S8)}$$

where K_w is the water permeability coefficient (mL atm^{-1} s^{-1} cm^{-1}), A_m is the effective membrane area, l is the membrane thickness, τ is the van't Hoff factor, R is the ideal gas constant, T is the temperature, and ΔC is the concentration gradient. A negligible hydraulic force was assumed in this system.

The amount of water consumed by the electrochemical water splitting process ($F_{consumed}$) can be determined using by the following equation:

$$F_{consumed} = \frac{iV_m}{2F} \quad \text{(S9)}$$

where i is the current, V_m is the molar volume of water, and F is Faraday's constant. For steady-state conditions where the volume within the cell is constant, F_{influx} and $F_{consumed}$ are equivalent, according to the equation (S10):

$$i/\Delta C = (\tau RT)(\frac{K_w A}{l})(\frac{2F}{V_m}) \quad \text{(S10)}$$

The van't Hoff factor τ and water permeability coefficient K_w can be estimated by measuring the water flux (0.026 mL h^{-1}) through the MoS_2 membrane with the same surface area and concentration gradient (feed side: 0.6 M NaCl, draw side: 0.8 M NaH_2PO_4). Thus, the current required for water splitting was calculated as ~63 mA. A slightly higher current of 76 mA was applied to attain a steady state. Because of the high water/ion selectivity of the C-MoS_2 membrane, the crossover flux for phosphate (P_i) and Cl^- were only 0.39 and 0.13 μmol h^{-1}, respectively. Less than 0.24 μmol of $HClO^-$/ClO^- oxidized from Cl^- was accumulated in the cell, accounting for the negligible Faradaic efficiency loss. Additionally, minimal gas-cross-over or other parasitic reductive and oxidative processes were found to compete with the electrochemical water splitting reactions. Our C-MoS_2-0.26 membrane demonstrated an energy storage (in H_2) efficiency of 43.68 kJ h^{-1} cm^{-2} via H_2 generation; this value is nearly 40 times higher than that of the reported commercialized cellulose acetate membranes[65].

Supplementary Note 4. Analysis of selective proton transport through the C-MoS_2 membrane

The proton transport through C-MoS_2-0.26 was investigated using three HCl concentration pairs, each with a four-fold concentration difference, including 0.4 M / 0.1 M, 0.2 M / 0.05 M, and 0.1 M / 0.025 M (Supplementary Fig. 21). The current at zero voltage was always positive,

indicating that protons predominantly drive the system toward equilibrium to equalize the proton concentrations in the two reservoirs[66]. In addition, the zero-current voltage (V_0) for the three *I–V* curves were nearly the same, $V_0 = 35 \pm 3.9$ mV. According to the Nernst equation[66,67]:

$$V_0 = (t_H - t_{Cl}) \left(\frac{kT}{e}\right) \ln(\Delta) \quad \text{(S11)}$$

where t_H and t_{Cl} are the transference numbers for H^+ and Cl^-, respectively, *k* is the Boltzmann constant, *T* is the temperature (~295 K in our experiments), and *e* is the elementary charge. For $\Delta = 4$ and $V_0 = $ ~35 mV, we obtain $t_H - t_{Cl} \approx 0.99$, indicating that most of the Cl^- ions were rejected and protons dominated the net current.

The diffusive proton permeability P_p can be estimated using the following equation[66]:

$$P_p = \left(\frac{G'L}{A}\right)\left(\frac{kT}{eFC_p}\right) \quad \text{(S12)}$$

where *G'* is the conductance, *L* is the membrane thickness, *A* is the effective membrane area, *F* is the Faraday constant, and C_p is the proton concentration. The effective membrane area was estimated based on a pore density of ~7.6×10^{11} per cm^2, and C_p (0.1 M) was used because of the nearly perfect rejection of Cl^-. Therefore, the estimated P_p was ~1×10^{-4} cm^2 s^{-1}, which was higher than that of two-dimensional monolayer water (~4×10^{-6} cm^2 s^{-1}, confined in two-dimensional graphene capillaries) and bulk water (~9×10^{-5} cm^2 s^{-1}) and of the same order for that of a one-dimensional single-file water chain (~4×10^{-4} cm^2 s^{-1}, confined in 0.8 nm CNTs)[66,68]. In three-dimensional bulk water, the average number of H bonds for each water molecule is larger than 3 but smaller than 4 [69]. According to the Grotthuss mechanism[70], an oxygen atom at the defect site can accept an “excess” proton and then pass it to the next water molecule. This step is followed by reorientations of the molecules, which is considered as a relatively slow step. For a two-dimensional monolayer water, each water molecule has four H bonds, because of which transferring excess protons between the molecules and rotating the water molecules becomes difficult[66]. In a one-dimensional single-file water chain, each water molecule has only two H bonds, and thus, a one-dimensional single-file water chain can easily accept and pass excess protons[68,71]. In our case, the C-MoS_2 membranes with 8-MR pores exhibited a thickness of ~0.7 nm, which can accommodate a short one-dimensional single-file water chain (~three water molecules in length) and thus shows less stable H bonds compared with those in the long water chains confined in CNTs. As a result, proton transport was slower than that observed in CNTs[68]. The pores larger than 1 nm (accounting for <2.3 %) in C-MoS_2-0.26 contributed negligibly to the highly selective proton conduction, because their selectivity for protons/metal ions is lower than 2 [72].

References

1 O'Hern, S. C. *et al.* Nanofiltration across defect-sealed nanoporous monolayer graphene. *Nano Lett.* **15**, 3254-3260, (2015).

2 Cheng, C., Lyengar, S. A. & Karnik, R. Molecular size-dependent subcontinuum solvent permeation and ultrafast nanofiltration across nanoporous graphene membranes. *Nat. Nanotech.* **16**, 989-995, (2021).

3 Graf, M. *et al.* Fabrication and practical applications of molybdenum disulfide nanopores. *Nat. Protoc.* **14**, 1130, (2019).

4 Shen, J. *et al.* Fast water transport and molecular sieving through ultrathin ordered conjugated-polymer-framework membranes. *Nat. Mater.* **21**, 1183-1190, (2022).

5 Perdew, J. P., Burke, K. & Ernzerhof, M. Generalized gradient approximation made simple. *Phys. Rev. Lett.* **77**, 3865-3868, (1996).

6 Kresse, G. & Furthmüller, J. Efficiency of ab-initio total energy calculations for metals and semiconductors using a plane-wave basis set. *Comput. Mater. Sci.* **6**, 15, (1996).

7 Bertoldo, F. *et al.* Intrinsic defects in MoS_2 grown by pulsed Laser deposition: from monolayers to bilayers. *ACS Nano* **15**, 2858-2868, (2021).

8 Gao, N., Guo, Y., Zhou, S., Bai, Y. & Zhao, J. Structures and magnetic properties of MoS_2 grain boundaries with antisite defects. *J. Phys. Chem. C* **121**, 12261-12269, (2017).

9 Abraham, M. J. *et al.* GROMACS: High performance molecular simulations through multi-level parallelism from laptops to supercomputers. *SoftwareX* **1-2**, 19-25, (2015).

10 Jorgensen, W. L., Maxwell, D. S. & Tirado-Rives, J. Development and testing of the opls all-atom force field on conformational energetics and properties of organic liquids. *J. Am. Chem. Soc.* **118**, 11225-11236, (1996).

11 Jorgensen, W. L., Chandrasekhar, J., Madura, J. D., Impey, R. W. & Klein, M. L. Comparison of simple potential functions for simulating liquid water. *J. Chem. Phys.* **79**, 926, (1983).

12 Luan, B. & Zhou, R. Wettability and friction of water on a MoS_2 nanosheet. *Appl. Phys. Lett.* **108**, 131601, (2016).

13 Essmann, U. *et al.* A smooth particle mesh Ewald method. *J. Chem. Phys.* **103**, 8577-8593, (1995).

14 Slater, J. C. Atomic radii in crystals. *J. Chem. Phys.* **41**, 3199-3204, (1964).

15 Chen, W. *et al.* Oxygen-assisted chemical vapor deposition growth of large single-crystal and high-quality monolayer MoS_2. *J. Am. Chem. Soc.* **137**, 15632-15635, (2015).

16 Yu, H. *et al.* Wafer-scale growth and transfer of highly-oriented monolayer MoS_2 continuous films. *ACS Nano* **11**, 12001, (2017).

17 Zhang, J. *et al.* Scalable growth of high-quality polycrystalline MoS_2 monolayers on SiO_2 with tunable grain sizes. *ACS Nano* **8**, 6024-6030, (2014).

18 Najmaei, S. *et al.* Vapour phase growth and grain boundary structure of molybdenum disulphide atomic layers. *Nat. Mater.* **12**, 754-759, (2013).

19 van der Zande, A. M. *et al.* Grains and grain boundaries in highly crystalline monolayer molybdenum disulphide. *Nat. Mater.* **12**, 554-561, (2013).

20 Liang, B. *et al.* Microporous membranes comprising conjugated polymers with rigid backbones enable ultrafast organic-solvent nanofiltration. *Nat. Chem.* **10**, 961-967, (2018).

21 Islam, Z. & Haque, A. Defects and grain boundary effects in MoS_2: A molecular dynamics study. *Journal of Physics and Chemistry of Solids* **148**, 109669, (2021).

22 Dang, K. Q. & Spearot, D. E. Effect of point and grain boundary defects on the mechanical behavior of monolayer MoS_2 under tension via atomistic simulations. *J. Appl. Phys.* **116**, 013508, (2014).

23 Wu, J. *et al.* Topology and polarity of dislocation cores dictate the mechanical strength of monolayer MoS_2. *Appl. Mater. Today* **15**, 34-42, (2019).

24 Abraham, J. *et al.* Tunable sieving of ions using graphene oxide membranes. *Nat. Nanotech.* **12**, 546-550, (2017).

25 Chen, L. *et al.* Ion sieving in graphene oxide membranes via cationic control of interlayer spacing. *Nature* **550**, 380-383, (2017).
26 Qian, Y. *et al.* Enhanced ion sieving of graphene oxide membranes via surface amine functionalization. *J. Am. Chem. Soc.* **143**, 5080-5090, (2021).
27 Shi, J. *et al.* Monolayer MoS_2 growth on Au foils and on-site domain boundary imaging. *Adv. Mater.* **25**, 842-849, (2015).
28 Deng, M., Kwac, K., Li, M., Jung, Y. & Park, H. G. Stability, molecular sieving, and ion diffusion selectivity of a lamellar membrane from two-dimensional molybdenum disulfide. *Nano Lett.* **17**, 2342-2348, (2017).
29 Sapkota, B. *et al.* High permeability sub-nanometre sieve composite MoS_2 membranes. *Nat. Commun.* **11**, 2747, (2020).
30 Ries, L. *et al.* Enhanced sieving from exfoliated MoS_2 membranes via covalent functionalization. *Nat. Mater.* **18**, 1112-1117, (2019).
31 Yang, Y. *et al.* Large-area graphene-nanomesh/carbon-nanotube hybrid membranes for ionic and molecular nanofiltration. *Science* **364**, 1057-1062, (2019).
32 Lokesh, M., Youn, S. K. & Park, H. G. Osmotic transport across surface functionalized carbon nanotube membrane. *Nano Lett.* **18**, 6679-6685, (2018).
33 Lu, Z. *et al.* Self-crosslinked MXene ($Ti_3C_2T_x$) membranes with good antiswelling property for monovalent metal ion exclusion. *ACS Nano* **13**, 10535-10544, (2019).
34 Ding, L. *et al.* Effective ion sieving with $Ti_3C_2T_x$ MXene membranes for production of drinking water from seawater. *Nat. Sustain.* **3**, 296-302, (2020).
35 Jian, M. *et al.* Ultrathin water-stable metal-organic framework membranes for ion separation. *Sci. Adv.* **6**, eaay3998, (2020).
36 Pang, J. *et al.* Exploring the sandwich antibacterial membranes based on UiO-66/graphene oxide for forward osmosis performance. *Carbon* **144**, 321-332, (2019).
37 Ma, D., Peh, S. B., Han, G. & Chen, S. B. Thin-film nanocomposite (TFN) membranes incorporated with super-hydrophilic metal–organic framework (MOF) UiO-66: Toward enhancement of water flux and salt rejection. *ACS Appl. Mater. Interfaces* **9**, 7523-7534, (2017).
38 Ma, N., Wei, J., Liao, R. & Tang, C. Y. Zeolite-polyamide thin film nanocomposite membranes: Towards enhanced performance for forward osmosis. *J. Membr. Sci.* **405-406**, 149-157, (2012).
39 Lu, P. *et al.* Layered double hydroxide/graphene oxide hybrid incorporated polysulfone substrate for thin-film nanocomposite forward osmosis membranes. *RSC Adv.* **6**, 56599-56609, (2016).
40 Ren, J. & McCutcheon, J. R. A new commercial thin film composite membrane for forward osmosis. *Desalination* **343**, 187-193, (2014).
41 Hu, M. & Mi, B. Enabling graphene oxide nanosheets as water separation membranes. *Environ. Sci. Technol.* **47**, 3715-3723, (2013).
42 Han, Y., Xu, Z. & Gao, C. Ultrathin graphene nanofiltration membrane for water purification. *Adv. Funct. Mater.* **23**, 3693, (2013).
43 Han, Y., Jiang, Y. & Gao, C. High-flux graphene oxide nanofiltration membrane intercalated by carbon nanotubes. *ACS Appl. Mater. Interfaces* **7**, 8147-8155, (2015).
44 Morelos-Gomez, A. *et al.* Effective NaCl and dye rejection of hybrid graphene oxide/graphene layered membranes. *Nat. Nanotech.* **12**, 1083-1088, (2017).
45 Zhang, W.-H. *et al.* Graphene oxide membranes with stable porous structure for ultrafast water transport. *Nat. Nanotech.* **16**, 337-343, (2021).
46 Li, L., Liu, N., McPherson, B. & Lee, R. Enhanced water permeation of reverse osmosis through MFI-type zeolite membranes with high aluminum contents. *Ind. Eng. Chem. Res.* **46**, 1584-1589, (2007).
47 Liu, X., Demir, N. K., Wu, Z. & Li, K. Highly water-stable zirconium metal–organic framework UiO-66 membranes supported on alumina hollow fibers for desalination. *J. Am. Chem. Soc.* **137**, 6999-7002, (2015).

48 Zhang, Y. *et al.* Molecularly soldered covalent organic frameworks for ultrafast precision sieving. *Sci. Adv.* **7**, eabe8706, (2021).
49 Yang, H. *et al.* Covalent organic framework membranes through a mixed-dimensional assembly for molecular separations. *Nat. Commun.* **10**, 2101, (2019).
50 Tan, Z., Chen, S., Peng, X., Zhang, L. & Gao, C. Polyamide membranes with nanoscale Turing structures for water purification. *Science* **360**, 518-521, (2018).
51 Jiang, Z., Karan, S. & Livingston, A. G. Water transport through ultrathin polyamide nanofilms used for reverse osmosis. *Adv. Mater.* **30**, 1705973, (2018).
52 Foglia, F. *et al.* Neutron reflectivity and performance of polyamide nanofilms for water desalination. *Adv. Funct. Mater.* **27**, 1701738, (2017).
53 Lin, J. *et al.* A comprehensive physico-chemical characterization of superhydrophilic loose nanofiltration membranes. *J. Membr. Sci.* **501**, 1-14, (2016).
54 Tang, Y.-J., Xu, Z.-L., Xue, S.-M., Wei, Y.-M. & Yang, H. A chlorine-tolerant nanofiltration membrane prepared by the mixed diamine monomers of PIP and BHTTM. *J. Membr. Sci.* **498**, 374-384, (2016).
55 Ali, Z. *et al.* Finely tuned submicroporous thin-film molecular sieve membranes for highly efficient fluid separations. *Adv. Mater.* **32**, 2001132, (2020).
56 Lear, J. D., Wasserman, Z. R. & DeGrado, W. F. Synthetic amphiphilic peptide models for protein ion channels. *Science* **240**, 1177-1181, (1988).
57 Weiss, L. A., Sakai, N., Ghebremariam, B., Ni, C. & Matile, S. Rigid rod-shaped polyols: Functional nonpeptide models for transmembrane proton channels. *J. Am. Chem. Soc.* **119**, 12142-12149, (1997).
58 Matsuki, Y. *et al.* Rectified proton grotthuss conduction across a long water-wire in the test nanotube of the polytheonamide B channel. *J. Am. Chem. Soc.* **138**, 4168-4177, (2016).
59 Li, X. *et al.* Sulfonated sub-1-nm metal–organic framework channels with ultrahigh proton selectivity. *J. Am. Chem. Soc.* **142**, 9827-9833, (2020).
60 Thiruraman, J. P., Masih Das, P. & Drndić, M. Stochastic ionic transport in single atomic zero-dimensional pores. *ACS Nano* **14**, 11831-11845, (2020).
61 Lipatov, A. *et al.* Elastic properties of 2D $Ti_3C_2T_x$ MXene monolayers and bilayers. *Sci. Adv.* **4**, eaat0491, (2018).
62 Lee, C., Wei, X., Kysar, J. W. & Hone, J. Measurement of the elastic properties and intrinsic strength of monolayer graphene. *Science* **321**, 385-388, (2008).
63 Liu, K. *et al.* Elastic properties of chemical-vapor-deposited monolayer MoS_2, WS_2, and their bilayer heterostructures. *Nano Lett.* **14**, 5097-5103, (2014).
64 Bertolazzi, S., Brivio, J. & Kis, A. Stretching and breaking of ultrathin MoS_2. *ACS Nano* **5**, 9703-9709, (2011).
65 Veroneau, S. S. & Nocera, D. G. Continuous electrochemical water splitting from natural water sources via forward osmosis. *Proc. Natl. Acad. Sci. U.S.A.* **118**, e2024855118, (2021).
66 Gopinadhan, K. *et al.* Complete steric exclusion of ions and proton transport through confined monolayer water. *Science* **363**, 145-148, (2019).
67 Helfferich, F. G. Ion Exchange: McGraw-Hill New York. *Chem. Eng. Sci.* **18**, 218, (1962).
68 Tunuguntla, R. H., Allen, F. I., Kim, K., Belliveau, A. & Noy, A. Ultrafast proton transport in sub-1-nm diameter carbon nanotube porins. *Nat. Nanotech.* **11**, 639-644, (2016).
69 Kumar, R., Schmidt, J. R., Skinner, J. L. & H., S. F. Hydrogen bonding definitions and dynamics in liquid water. *J. Chem. Phys.* **126**, 204107, (2007).
70 Marx, D., Tuckerman, M. E., Hutter, J. & Parrinello, M. The nature of the hydrated excess proton in water. *Nature* **397**, 601-604, (1999).
71 Tunuguntla, R. H. *et al.* Enhanced water permeability and tunable ion selectivity in subnanometer carbon nanotube porins. *Science* **357**, 792-796, (2017).
72 Griffin, E. *et al.* Proton and Li-ion permeation through graphene with eight-atom-ring defects. *ACS Nano* **14**, 7280-7286, (2020).